Tissue-specific and spatially dependent metabolic signatures perturbed by injury in skeletally mature male and female C57Bl/6J mice

Hope D. Welhaven[1], Avery H. Welfley[2], Priyanka P. Brahmachary[2], Donald F. Smith, Brian Bothner1, *Ronald K. June[2]

Affiliations
[1]Department of Chemistry & Biochemistry, Montana State University, Bozeman MT
[2]Department of Mechanical & Industrial Engineering, Montana State University, Bozeman MT.
Corresponding Author: Ronald K. June, E-mail: rjune@montana.edu

Abstract

Injury is a risk factor for post-traumatic osteoarthritis (PTOA). However, metabolic and microarchitectural changes within the joint post-injury in both sexes remain unexplored. This study identified tissue-specific and spatially-dependent metabolic signatures in male and female mice using matrix-assisted laser desorption ionization-mass spectrometry imaging (MALDI-MSI) and metabolomics. Male and female C57Bl/6J mice were subjected to non-invasive joint injury. Eight days post-injury, serum, synovial fluid, and whole joints were collected for metabolomics to compare samples from injured, contralateral, and naïve mice, revealing local and systemic responses. Results indicate sex influences metabolic profiles across all tissues, particularly amino acid, purine, and pyrimidine metabolism. MALDI-MSI generated 2D ion images of bone, growth plate, and marrow, revealing increased lipid species in injured limbs, suggesting metabolic shifts across injured joints at metabolic and spatial levels. Together, these findings reveal significant metabolic changes after injury, with notable sex differences.

Introduction

Post-traumatic osteoarthritis (PTOA) accounts for 12% of all osteoarthritis (OA) cases, equating to 5.6 million cases annually[1, 2]. The most prevalent risk factor for PTOA is joint injury. The annual incidence rate of anterior cruciate ligament (ACL) injuries is 250,000, commonly occurring in individuals between the ages of 16 and 24. Unfortunately, upwards of 50% of patients will develop PTOA within 10-20 years of injury[3-6]. Additionally, a noteworthy PTOA risk factor is sex. Young female athletes are two to eight times more likely to sustain a traumatic knee injury requiring surgical repair compared to their male counterparts[7, 8]. Following repair, female athletes experience greater joint instability and physiological stress and have a 25% less chance of returning to their sport within 5 years compared to male athletes[8-10]. Later in life, females are more likely to develop OA and often experience greater symptom severity[11, 12]. This sexual dimorphism can be boiled down to anatomical and hormonal differences where females have wider pelves, smaller femurs, different muscle angles, and physically smaller ACLs[13, 14]. Despite these empirical sex differences, many studies fail to include both female and male subjects and, specific to sports, male-dominated sports are typically focused on.

Preclinical mouse models have improved the field's understanding of PTOA where PTOA can be induced through ACL destabilization of the medial meniscus (DMM), intraarticular injection to induce degradation, or ACL transection[15]. Each is met with challenging procedures and often fails to fully replicate in vivo pathophysiology. A non-invasive PTOA model, involving tibial compression overload, has been shown to simulate clinical ACL tears where natural joint

processes occurring at the early time points after injury are observed[15-18]. A handful of studies have employed this non-invasive PTOA model and have observed changes in musculoskeletal tissues post-injury at different time scales. Specifically, changes in trabecular bone have been detected within 7 days post-injury using microCT[16] and synovial fluid (SF) and serum metabolism has been shown to rapidly shift after injury (days 1 and 7 post-injury)[19].

While it is well known that injury and sex are prevalent PTOA risk factors, underlying mechanisms and changes in metabolism and microarchitecture following injury remain incompletely understood. Thus, preclinical models can be leveraged to examine acute differences in response to injury at different time scales and across various tissues using mass spectrometry-based approaches. Metabolomics – the study of small molecule intermediates called metabolites – captures the physiological and metabolic status of the joint. While SF and serum have been assessed post-injury in human and mouse models[19-23], metabolomics can also be applied to whole joint tissue to characterize metabolic changes occurring in bone and cartilage post-injury. We hypothesize that a metabolomic assessment of all three tissues in injured and naïve male and female mice will reveal metabolic shifts that are both unique and conserved across tissues. Once characterized, these markers could be measured through SF needle biopsy or simple bloodwork in the clinical setting to improve post-injury care. Moreover, investigating all three tissues post-injury will shed light on whether shifts in metabolism parallel pathological changes in bone.

A second mass spectrometry-based approach is matrix-assisted laser desorption ionization-mass spectrometry imaging (MALDI-MSI). This technique produces a two-dimensional chemical map that can spatially locate and detect differences in osteochondral metabolites that compose the mouse knee joint. MALDI-MSI is a powerful tool that can complement traditional measurements used to examine cartilage and bone, as it spatially resolves and characterizes molecular species in a single molecular imaging experiment in a label-free way[24]. By capturing spatial and temporal information with high resolution, the molecular aspects of injury on the joint can be examined[25, 26]. A small handful of studies have applied MALDI-MSI to study musculoskeletal tissues such as cartilage[27, 28] and synovium[29], however, no study to date has utilized MALDI-MSI to characterize molecular changes between male and female injured and naïve mice.

The first objective of this study was to characterize metabolomic differences within and across whole joints, SF, and serum from injured and naïve male and female mice using liquid chromatography-mass spectrometry (LC-MS). Investigating differences in metabolism in different tissues and between injured, contralateral, and naïve limbs is important as it will shed light on both local and systemic metabolic responses following injury. The second objective of this study was to spatially locate and identify osteochondral metabolites using MALDI-MSI. By combining untargeted metabolomic profiling and MALDI-MSI, we can pinpoint the origin of metabolic and pathological shifts and gain a better understanding of the effects of injury and sex on the joint as a whole.

Results

Injury Perturbs the Metabolome Across Whole Joints, Synovial Fluid, and Serum

In total, 2,769 metabolite features were detected by LC-MS across all samples (n=92). First, whole joints, SF, and serum were assessed to determine if metabolomic profiles were distinct between tissues. Using PLS-DA, the metabolomes of whole joints, SF, and serum are substantially distinct when assessing either all samples (Fig. S1A) or only injured samples (Fig.

S1B). ANOVA analysis revealed 2,264 and 1,891 metabolite features that were significantly dysregulated across all samples and only injured samples, respectively (Fig. S1C-D).

To visualize, assess, and distinguish metabolic differences associated with injury within each sample type, PLS-DA, fold change, and volcano plot analyses were conducted. First, using PLS-DA, differences associated with injury were assessed in whole joint, SF, and serum (Fig. 1 A-C). When comparing injured and naïve whole joints and SF, some overlap is observed (Fig. 1 A-B), whereas distinct separation with no overlap is observed when comparing serum from injured and naïve mice (Fig. 1 C). To distinguish populations of metabolite features driving these differences, fold change analysis was performed (Fig. 1D-F).

Populations of features distinguished by fold change analysis were subjected to pathway analysis where 2 pathways – pantothenate and CoA biosynthesis and histidine metabolism – were highest in injured whole joints, whereas 5 pathways including various amino acid pathways and terpenoid backbone synthesis were highest in naïve whole joints (Table 1A). Features highest in injured SF compared to naïve mapped to 8 significant pathways including various amino acid pathways, glutathione metabolism, and pyrimidine metabolism. Conversely, features highest in naïve SF compared to injured mapped to 4 significant pathways including biosynthesis of unsaturated fatty acids, purine metabolism, terpenoid backbone biosynthesis, and valine, leucine, and isoleucine biosynthesis (Table 1B). Features highest in injured serum, compared to naïve serum, mapped to 5 significant pathways including 4 amino acid pathways and nicotinate and nicotinamide metabolism. Conversely, those highest in naïve serum, compared to injured serum, mapped to 11 significant pathways including purine and pyrimidine metabolism, vitamin B6 metabolism, glutathione metabolism, amino acid pathways, and various others (Table 1C). Volcano plot analysis, which combines both fold change and significance, identified numerous features that were highest in injured and naïve whole joints, SF, and serum (Fig. 1G-I). Features distinguished by volcano plot analysis were matched to metabolite identifications made using LC-MS/MS data to unveil potential metabolic indicators of injury (Table S1). Of these, 3,4-Dimethyl-5-pentyl-2-furanundecanoic acid was differentially regulated between naïve and injured whole joints, whereas numerous amino acid putative identified metabolites, such as D/L-glutamine, was highest in injured SF compared to naïve (Table S1).

Systemic Response Following Joint Injury Across Limbs in Whole Joints and Synovial Fluid

To further examine metabolic differences associated with injury - injured, contralateral, and naive whole joints and SF were examined. PLS-DA analysis of all three joint types revealed overlap, where the metabolome of injured whole joints and SF resides between contralateral and naïve whole joints and SF (Fig. 2A, C), suggesting metabolic differences associated with injury at the whole joint and SF levels are observed in the contralateral limb.

Next, a median intensity heatmap analysis normalized to naïve samples was performed to visualize and pinpoint clusters of metabolite features that are co-regulated and differentially expressed across limbs. Clusters of metabolite features were then subjected to pathway analyses. Comparing injured, contralateral, and naïve whole joints, 22 significant pathways were detected across 8 clusters (Fig. 2B, Table 2). Noteworthy pathways that were highest in injured joints, and similar in regulation in contralateral and naïve joints, mapped to glycerophospholipid metabolism (Cluster 3). Glutathione and purine metabolism were highest in injured whole joints, but lowest in contralateral joints (Cluster 4). Conversely, lysine degradation was highest in contralateral whole joints, and lower in injured and naïve whole joints (Cluster 5). Metabolite features that were higher in both injured and contralateral joints mapped to a handful of pathways

including amino acid pathways, biosynthesis of unsaturated fatty acids, porphyrin metabolism, and selenocompound metabolism (Clusters 6-8). Metabolite features lowest in both injured and contralateral whole joints compared to naïve joints mapped to nitrogen metabolism (Clusters 1, 2).

Similarly, metabolic shifts in SF following injury across limbs were assessed using a median heatmap analysis (Fig. 2D, Table 3). Metabolite features lowest in injury, but similar in regulation in contralateral and naïve SF, mapped to fructose and mannose metabolism, cysteine and methionine metabolism, taurine and hypotaurine metabolism, and pyruvate metabolism (Cluster 1). Metabolite features lowest in both injured and contralateral SF, compared to naïve SF, mapped to 5 pathways including amino acid pathways and purine metabolism (Cluster 2). Interestingly, metabolite features highest in contralateral SF, but similar in regulation in injured and naïve SF, mapped to sphingolipid metabolism and biosynthesis of unsaturated fatty acids (Cluster 3). Those highest in injured SF, but lower in contralateral and naïve SF, mapped to beta-alanine metabolism and glutathione metabolism (Cluster 5). Lastly, metabolite features relatively higher in both injured and contralateral SF, compared to naïve SF, mapped to pyrimidine metabolism and terpenoid backbone biosynthesis (Cluster 6). All pathways reported had an FDR-corrected $p < 0.05$.

Additionally, pairwise comparisons of injured, contralateral, and naïve whole joints and SF were performed to further examine the effects of injury across different joints (Fig. S3-4, Table Ss 2-3). The results of pairwise comparisons are further discussed in the Supplemental results. Collectively, the results of PLS-DA, fold change, volcano plot, and heatmap analysis strongly suggest that injury influences the whole joint and SF metabolome and produces a systemic response that influences both the injured and contralateral joints. Collectively, it is evident that injury perturbs metabolism spanning the whole joint, SF, and serum. Moreover, the metabolome of injured, contralateral, and naïve limbs are metabolically distinct suggesting that injury has a systemic response that stretches beyond the injured joint itself.

Sex Influences Metabolomic Profiles Across Tissues of Injured and Naive Mice

To examine the effects of sex and its interactions with injury on the whole joint, SF, and serum metabolomes, a series of pairwise comparisons were performed. First, general sex differences were examined in male and female whole joints (Fig. S4) revealing distinct metabolomic profiles between sexes. Thus, whole joints from injured males and females were assessed using PLS-DA which revealed clear separation of mice within their respective cohorts (Fig. 3A). Similarly, injury differences are evident when comparing whole joints from injured and naïve females (Fig. 3B) and from injured and naïve males as seen by minimal PLS-DA overlap (Fig. 3C). Fold change analysis distinguished populations of metabolite features that are differentially regulated among injured male and female whole joints (Fig. 3D), injured and naïve females (Fig. 3E), and injured and naïve males (Fig. 3F). Populations of metabolite features distinguished by fold change analyses underwent pathway analyses.

Pathways that were highest in whole joints from injured males mapped to purine metabolism and alanine, aspartate, and glutamate metabolism. Conversely, pathways highest in whole joints from injured females mapped to cysteine and methionine metabolism, pyruvate metabolism, tyrosine metabolism, and vitamin B6 metabolism. Pathways that were consistent across whole joints from males regardless of injury status included arginine biosynthesis, beta-alanine metabolism, glycerophospholipid metabolism, primary bile acid biosynthesis, and sphingolipid metabolism. Lastly, pathways that were consistent across whole joints from females

included lysine degradation, terpenoid backbone biosynthesis, and valine, leucine, and isoleucine degradation (Table S4). To unveil metabolic indicators reflective of both injury and sex, volcano plot analysis was performed comparing whole joints from injured males and females (Fig. 3G), as well as injured and naïve females (Fig. 3H) and males (Fig. 3I). Putative metabolite identifications related to terpenoid backbone biosynthesis were identified including (6R)-6-(L-Erythro-1,2-Dihydroxypropyl)-5,6,7,8-tetrahydro-4a-hydroxypterin which was associated with whole joints from females. Notably, Sterebin E which is also associated with terpenoid backbone biosynthesis was associated with whole joints in males (Table S1).

The same series of analyses were performed to assess metabolic differences between injured and naïve male and female mice within SF and serum samples. Within SF, general sex differences were evident (Fig. S4). By employing PLS-DA, it is evident that the metabolome is influenced by both injury and sex where minimal overlap is observed between SF from injured males and females (Fig. 4A), naïve and injured females (Fig. 4B), and males (Fig. 4C). Fold change analysis distinguished populations of metabolite features that are differentially regulated among SF from injured males and females (Fig. 4D), injured and naïve females (Figure 4E), and injured and naïve males (Fig. 4F). These populations underwent pathway analyses revealing overlapping and distinctly regulated pathways across SF groups (Table S5). Specifically, phenylalanine metabolism was consistently higher in females compared to males, regardless of injury status. Pathways unique to SF from injured males mapped to alpha-linolenic acid metabolism, butanoate metabolism, TCA cycle, propanoate metabolism, and tryptophan metabolism. Conversely, those unique to SF from injured females mapped to arginine biosynthesis, glycerophospholipid metabolism, and pyrimidine metabolism. Unique to naïve females and males included beta-alanine metabolism and biosynthesis of unsaturated fatty acids. On the other hand, pathways unique to injured males and females included D-amino acid metabolism, glycine, serine and threonine metabolism, and lysine degradation. Lastly, a pathway that was differentially regulated between injured females and naïve males was histidine metabolism. To pinpoint metabolite features contributing to the observed sexual dimorphism, volcano plot analysis was performed comparing SF from injured males and females (Fig. 4G), as well as injured and naïve females (Fig. 4H) and males (Fig. 4I). Among those identified, 3-Methylhistamine was associated with females and was highest in injured SF, whereas D/L-Valine was associated with males and was highest in injured males (Table S1).

Lastly, serum was assessed in a similar way to determine if metabolomic differences were evident considering sex and injury. Like whole joint and SF analyses, comparing males and females, regardless of injury status, reveals evident sex differences. To delve deeper into the interactions of sex and injury at the level of serum, PLS-DA was performed and showcased extremely distinct separation of injured males and females (Fig. 5A). When controlling for sex, some overlap is present when comparing injured and naïve females (Fig. v5B) and males (Fig. 5C). Fold change distinguished populations of metabolite features that are differentially regulated between injured males and females (Fig. 5D), injured and naïve females (Fig. 5E), and males only (Fig. 5F).

These metabolite features were then subjected to pathway analyses, revealing numerous statistically significant pathways (Table S6). Those detected in females, regardless of injury status, included arginine and proline metabolism and pantothenate and CoA biosynthesis. Conversely, pathways detected in males, regardless of injury status, included cysteine and methionine metabolism, glycerophospholipid metabolism, nicotinate and nicotinamide metabolism, nitrogen metabolism, phenylalanine metabolism, and tyrosine metabolism.

Porphyrin metabolism was unique to injured males, whereas primary bile acid biosynthesis and pyrimidine metabolism were unique to injured females. Lastly, pathways that were repeatedly detected in injured mice, regardless of sex, mapped to alanine, aspartate, and glutamate metabolism, lysine degradation, and purine metabolism.

To examine metabolic differences beyond pathways, volcano plot analysis was performed comparing serum from injured males and females (Fig. 5G) as well as injured and naive females (Fig. 5H) and males only (Fig. 5I). Similar to SF, D/L-Valine was associated with males. Notably, 1/3-methyhistidine was associated with injury regardless of sex and was detected in the SF from injured females (Table S1).

Considering metabolic differences associated with sex and injury across all tissues – whole joints, SF, and serum – a handful of pathways are conserved. Alanine, aspartate, and glutamate metabolism were detected in whole joints of injured males and SF and serum of injured males and females. Arginine biosynthesis was detected among whole joints from males; however, it was detected in serum from injured females and SF from injured males and females. Beta-alanine, glyoxylate, and dicarboxylate metabolism were detected across all male naïve tissues. Cysteine and methionine metabolism was detected in both whole joint and SF from injured females. Interestingly, lysine degradation and pyrimidine metabolism were detected across all three tissues in injured females. Moreover, it was associated with injured males in SF and serum.

MALDI-MSI Spatially Locates and Detects Differences in Osteochondral Metabolites

To characterize and examine metabolites that are tissue-specific and compose the whole joint, MALDI-MSI was performed. A novel protocol encompassing sample preparation, matrix application, and instrumentation was developed to avoid losing metabolites (50-1500 m/z) that are typically removed during formalin fixation and paraffin embedding of bone (Fig. 7). In doing so, this allows for the visualization of the spatial distribution of metabolites, particularly focused on lipids. Different populations of metabolites were observed in different spatial areas of the joint – including cartilage, bone, and the growth plate – suggesting unique tissue-dependent metabolite signatures. Using LC-MS/MS derived metabolite identifications from whole joint samples, a handful of metabolites with unique spatial patterns were putatively identified (Fig. 6, Table S7). Those with notable spatial patterns amongst bone and the growth plate included alpha-carboxy-delta-decalactone (215.20 m/z), hydroxyprolyl-isoleucine (245.11 m/z), and $C_{36}H_{38}O_7$ (629.61 m/z) (Fig. 6, Fig. S5A). Conversely, metabolites with notable patterns among bone marrow regions included L-carnitine (162.29 m/z) and various lipid species (34 carbons, 2 double bonds – 758.57 m/z; 34 carbons bonds, 3 double bonds – 778.59 m/z; 39 carbons, 6 double bonds – 820.41 m/z) (Fig. 6, Fig. S5B). Many metabolites displayed unique spatial patterns among bone, growth plate, and bone marrow but were unable to be identified. However, many of these were within the common lipid m/z range (400-800 m/z) (Fig. S6, Table S7).

To investigate injury associated spatial patterns, ion images from the medial and lateral aspects of both the right and left mouse joints were examined. Upon assessing an injured mouse where the left limb was injured, 544.41 m/z and putatively identified metabolite - 36 carbons, 6 double bonds 878.54 m/z - display notable injury associated patterns between medial and lateral sagittal sections where they are more abundant in the injured joint compared to the contralateral joint (Fig. S7). Sex-associated patterns were not examined at length due to the limited number of joints allocated for MALDI-MSI (n = 1 mouse/group, n = 2 males, 2 females, n = 4 mice total).

Discussion

To our knowledge, this is the first study to examine structural and metabolic responses following injury in different tissues – whole joints, SF, and serum – using LC-MS metabolomic profiling and MALDI-MSI. The goals of this study were to (1) identify tissue-specific and spatially dependent metabolic signatures perturbed by injury and (2) pinpoint metabolic differences associated with sex. Metabolomic profiling has been used to profile SF following injury in mouse models as it reflects cartilage morphological changes, however, changes in bone are traditionally investigated using microCT, leaving key questions unanswered about the whole joint response.

Effects of injury across whole joints, synovial fluid, and serum

Distinct metabolomic profiles of whole joints, SF, and serum reveal acute changes occur in response to injury. Various amino acid pathways exhibit differential regulation across tissues with many overlapping between tissues. Lysine degradation displayed differential regulation across injured, contralateral, and naive whole joints (Table 6.1 A, Table 6.2) while being downregulated in SF contralateral and injured limbs compared to naïve (Table 6.3). Detection of this pathway may be associated with collagen, where lysine residues are crucial for collagen's structural integrity through hydroxylation and cross-link formation[30]. Specific to bone, collagen is a major component of the structural organic matrix and when lysyl hydroxylase levels are altered in osteoblasts, defective cross-linking patterns, fibrillogenesis, and matrix mineralization are observed[30-32] underscoring the importance of lysine hydroxylation in bone quality. In SF, lysine metabolism tends to decrease as OA progresses[33], suggesting this pathway could represent acute joint changes following injury that could be monitored to oversee joint health and disease.

Arginine and proline metabolism was upregulated in naïve whole joints and in injured SF (Table 6.1 A, B). Like lysine, proline is associated with collagen, where it contributes to collagen synthesis. Arginine has anti-inflammatory effects and has been shown to decrease in concentration as OA develops[34, 35]. Arginine and proline metabolism has been detected in rabbit SF post-ACL injury[36], in human SF from patients who sustained traumatic knee injuries[22], and in mouse serum 1-day post-ACL injury and decreased by day 7[19]. Combined, this may indicate a short-term protective mechanism, or cascade of pathways, to enhance ATP production post-injury. The detection of this pathway in SF from injured mice aligns with previous work, however, additional research is required to understand pathway regulation in bone post-injury.

Phenylalanine, tyrosine, and tryptophan biosynthesis exhibited differential regulation when comparing injured, contralateral, and naive limbs at the whole joint (Fig. 6.2 B, Cluster 6). And SF levels (Fig. 6.2 D, Cluster 2). While higher in injured and contralateral whole joints compared to naïve ones, these pathways showed the opposite trend in SF. These aromatic amino acids can bind to the calcium-sensing receptor, in turn raising intracellular calcium and modulating bone turnover[37]. Moreover, phenylalanine and tyrosine metabolism have been associated with the sclerosis of subchondral bone in OA[38]. In a noninvasive mouse injury model, tryptophan metabolism was higher in mouse SF 7 days post-injury compared to naïve controls. Tryptophan has been noted as a promising biomarker of OA where its concentration decreases as disease progresses[39, 40]. The detection of this pathway in both injured and contralateral whole joints is novel, suggesting a systemic response is produced in both injured and contralateral whole joints. Moreover, these results hold promise as amino acids in general have been shown to play a role in the response to acute injury[41], have been detected post-injury across mammalian models[19, 22, 36], and have been noted as molecules whose concentration changes with disease progression.

Purine and pyrimidine metabolism were detected across tissues from injured mice. Pyrimidine metabolism was highest in injured whole joints and injured and contralateral SF, while purine metabolism was highest in SF from naïve mice, but highest in serum from injured mice. Both pathways, derived from the pentose phosphate pathways, synthesize nucleotides and amino acids. Purigenic signaling, mediated by purine nucleotides like adenosine and ATP, contributes to OA pathophysiology, influencing processes such as cell proliferation, tissue regeneration, and inflammation[42-45]. Detection of these pathways provides insight into energy generation, inflammation, and signaling at the site of injury in both whole joints and SF.

Sexual dimorphism of injury among the metabolome of whole joints, synovial fluid, and serum

Considering both injury and sex, purine and pyrimidine metabolism showed dysregulated patterns. Purine metabolism was consistently detected across all tissues from injured males, particularly in serum, which could be explained given that uric acid—an end product of purine metabolism— is much higher in males compared to females[46] where female hormones decrease uric acid levels[47]. Conversely, pyrimidine metabolism was dominant in tissues from injured females, necessitating further research to understand its sexual dimorphic regulation.

Dysregulated glycine, serine, and threonine metabolism was detected in serum and SF in injured males and females. In a previous study on female sheep post-ACL injury, this pathway was notably perturbed among injured animals with serine identified as a potential biomarker for early degenerative changes[21]. Serine, a glucogeneic amino acid, influences adenosine monophosphate kinase (AMPK), which acts as a key “energy sensor” that maintains energy homeostasis and promotes ATP synthesis, via serine/threonine phosphorylation[48-50]. Mechanisms like AMPK are differentially influenced by circulating sex hormones like estrogen which can bind to estrogen receptor beta, triggering downstream metabolic cascades to generate ATP[51, 52]. The influence of circulating sex hormones, like estrogen, on mechanisms like AMPK may affect energy metabolism post-injury, warranting further investigation into sexual dimorphic patterns.

Cysteine and methionine metabolism was highest in whole joints and SF from injured females but in serum from injured males. Histidine metabolism was higher in injured males in serum and whole joints but in injured females at the SF level. These three amino acids are related to matrix metalloproteinases (MMPs) regulate tissue remodeling and degradation of extracellular matrix proteins, cell proliferation, and immune responses[53]. MMP activation is modulated by a cysteine switch and the catalytic domain of MMPs is regulated by these amino acids because zinc binds to histidines with assistance from conserved methionine sequences[53, 54]. MMP activity has been shown to be influenced by hormones[55], like estrogen and progesterone, particularly in chondrocytes. In a previous study, chondrocytes from 25 postmenopausal OA patients were cultured with different concentrations of 17B-estradiol and found that physiological levels of estrogen suppressed the expression of MMP-1 and that hormone replacements could benefit female OA patients in the early stages of disease[56]. Thus, differential regulation of AMPK and MMP-associated amino acids between males and females’ post-injury suggests reliance on different metabolic pools, mechanisms, and biofuels to meet energy demands and maintain matrix properties following joint injury. Further investigation into amino acid concentrations at different tissue levels and between males and females is needed to understand metabolic differences associated with injury site versus circulating serum.

MALDI-MSI Provides New Insight into Composition of Osteochondral Tissue at the Metabolite Level

To our knowledge, this is the first study to examine the spatial distribution of osteochondral metabolites, with an emphasis on lipids, following joint injury. Here, we developed an innovative protocol to localize and spatially locate osteochondral metabolites that compose whole joints from injured and naïve mice using MALDI-MSI. Only a handful of studies have employed MALDI-MSI in musculoskeletal tissues, with many being in human samples, to visualize the spatial distribution of proteins and peptides[26, 29, 33, 57]. While many of these studies have provided the field with a new tool to study these tissues, findings are narrowed to these larger molecules. Traditionally, histological sectioning and imaging of whole joints – and bone samples in general – first require formalin fixation and paraffin embedding to preserve and demineralize the bone. However, this can result in removal, cross-linking, or delocalization of molecular species, especially lipid species[58], leading us to develop this novel protocol to include these species.

Lipid metabolism has become increasingly recognized for its role in the development of PTOA and OA. Proteomic and metabolomic studies have revealed a significant relationship between OA and lipid metabolism through the analysis of SF, cartilage, bone, and circulatory fluids in both humans and mice[27, 33, 59-62]. Consequently, employing MALDI-MSI to target small molecules (50-1500 m/z) offers crucial insights into joint composition, specifically in relation to lipid dynamics and their changes post-injury. In this study, MALDI-MSI successfully mapped and detected differences in osteochondral metabolites, with many identified as lipid species. Notably, it detected injury-related ions, such as PC(14:0/22:6) (m/z 878). The MALDI-MSI findings align with metabolomic assessments where lipid-associated pathways – such as glycerophospholipid metabolism and the biosynthesis of unsaturated fatty acids – in injured joints compared to naive and contralateral joints. Consistent with our previous analysis of metabolic phenotypes of early PTOA in SF[23, 33, 57, 63] and in OA cartilage[62, 64], dysregulated lipid metabolism has been linked to both early-stage PTOA and end-stage OA, suggesting similar metabolic shifts occur in the joint at the metabolic and spatial levels. This underscores the need for further research into lipid metabolism's role in both local and systemic changes following injury and during early PTOA development. Together, this two-pronged approach utilizing LC-MS-based metabolomics and MALDI-MSI sheds light on the importance of lipids in joint metabolism, both globally and spatially. Moving forward, MALDI-MSI at the level of proteins, peptides, and lipids can be leveraged and integrated with existing techniques to enhance our understanding of the joint's post-injury response across multiple length scales.

Our study has notable limitations. Firstly, this study focused on the early response to joint injury where mice were euthanized at 8 days post-injury. Additional time points within the first 7 days of injury as well as upwards of 56 days post-injury[16] may shed light on the arc of structural and metabolic changes across serum, SF, and whole joints. Secondly, while multiple samples were obtained from each mouse, sample size was small (N=20, n=5/group). Thirdly, metabolite extraction protocols and use of HILIC column bias data toward the assessment of polar molecules. Moreover, DHB was used for MALDI-MSI, which is optimal for positive ionization mode. Combined, LC-MS and MALDI-MSI analyses were both conducted in positive ionization mode focusing on polar molecules, thus additional investigation into nonpolar species is warranted.

The findings of our study, integrating LC-MS-based metabolomics and MALDI-MSI, underscore significant metabolic and pathological shifts following joint injury, with discernible

sex-specific associations. The detection of novel differences associated with both injury and sex across serum, SF, and whole joints enhances our current understanding of the post-injury response within and beyond the joint. Moreover, it is evident that the whole joint is influenced by injury at multiple length scales, further supported by differences in the SF metabolome, suggesting a systemic response is produced in both injured and contralateral joints. Further investigation into molecules perturbed by injury in males and females, at the level of the metabolome and spatially, is imperative for pinpointing the effects of injury comprehensively. Completion of this work has the potential to refine and improve pre-clinical PTOA models and deepen our insights into PTOA development, thereby advancing strategies for prevention and treatment.

Materials and Methods

Animals

C57Bl/6J male and female mice (N=20, n = 10 female, n = 10 male) were utilized to compare the spatial and metabolic effects of injury and sex on the whole joints, SF, and serum. Mice were purchased from Charles River Laboratories at 18 weeks of age and acclimated to the Montana State University Animal Research Center for 3 weeks. All mice were housed in cages of 3-5 mice and fed standard chow-fed diet ad libitum (PicoLab Rodent Diet 20, 20% protein). All animal procedures were approved by the Institutional Animal Care and Use Committee at Montana State University.

Joint Injury Model and Experimental Design

Once acclimated, mice were randomly assigned to experimental groups: injured or non-injured. Those assigned to the injury group were subjected to a non-invasive injury model where the ACL is ruptured in a way that closely mimics ACL rupture in humans, an injury associated with degeneration of bone and cartilage[15, 65]. Historically, this model begins to display changes in subchondral trabecular bone at 7 days[16]. Thus, experimental groups are as follows with five mice in each group: male injured mice, male uninjured mice, female injured mice, and female uninjured mice.

On the day of injury, mice were anesthetized using isoflurane inhalation. Mice were then placed in the custom-built tibial compression system where a single compressive overload to the lower leg was applied (target force = 12N, loading rate = 130 mm/s)[20]. The injured side was also randomized for mice assigned to injury groups. After 8 days, all mice were euthanized via cervical dislocation followed by a thoracotomy. Samples collected included both whole joints, SF, and serum from every mouse. Whole joints were harvested, all soft tissue was removed, and were stored intact. SF was recovered and then extracted using established protocols[66], with some modifications. To access the SF, skin was removed from the leg, and using a scalpel, the tibial plateau was palpated to identify the joint line. Next, an anterior incision was made through the patellar tendon then retracted to access the joint capsule where a second incision was made to access the SF via Whatman paper (Sigma, WHA1441042). Once saturated, Whatman paper with adsorbed SF was placed in a 1.5 mL microcentrifuge tube where 150 uL of 80:20 methanol:H2O was added. Blood samples were obtained by cardiac puncture, collected in a standard red top serum tube microtainer (BD Microtainer Red Tubes No Additive, 365963), inverted six times, then incubated at room temperature for 60 minutes to activate clotting factors. Serum samples were centrifuged at 2000 x g for 10 minutes at 4°C to remove cells and remaining clotting factors. Resulting supernatant designated as serum was transferred to a clean 1.5 mL microcentrifuge tube. All samples were stored at -80°C until metabolite extraction.

Metabolomics

Metabolite Extraction and Mass Spectrometry Instrumentation

Whole joints selected for metabolomic analysis were removed from -80°C, allowed to thaw over ice, and disarticulated to separate the tibia and femur. The distal end of the tibia and proximal end of the femur were trimmed and centrifuged for 5 minutes at 16,100 x g at 4°C to remove bone marrow. Next, bones were combined in one homogenization tube, precipitated with 1 mL of 80:20 methanol:H2O, and homogenized using a tissue homogenizer (1200 GenoLyte, Fischer Scientific). Following homogenization, whole joint samples were placed at -20°C overnight.

The next day, SF and serum were centrifuged for 5 minutes at 500 x g at 4°C to remove cells and debris. Supernatant was transferred and three times the volume 80:20 methanol:H2O was added. Upon vortexing for 3 minutes, samples were chilled at -20°C for 30 minutes. At this point, all samples including whole joint, SF, and serum samples were extracted the same and together. Thus, all samples were removed from -20°C, centrifuged for 5 minutes at 16,100 x g at 4°C, and supernatant was dried via vacuum concentration. To remove any remaining proteins, as well as lipids and waxes, dried extracts were then resuspended with 250 uL of 1:1 acetonitrile:H2O, vortexed, chilled at -20°C for 30 minutes, and centrifuged again for 5 minutes at 16,100 x g at 4°C. Supernatant was dried once more and once dried, extracts were prepped for LC-MS using 100 uL of 1:1 acetonitrile:water. Additionally, pooled samples were generated by randomly pooling a total of 50 uL for each tissue type (n=4/tissue), then pooled samples from each tissue type were also pooled for identification purposes. All solvents used were mass spectrometry HPLC grade (Fischer Scientific).

All samples, including extracted tissues and pools, were analyzed via LC-MS as previously described[22]. In brief, a Waters Acquity I-Class UPLC was interfaced via an electrospray ionization source (positive mode) to a Waters Synapt XS. For chromatography, an Acquity Waters HILIC column (150 x 2.1mm) at a flow rate of 0.400 uL/min was utilized to separate metabolites over a 12-minute gradient (A=95/5% water/acetonitrile, B = 95/5% acetonitrile/water). Every 10 injections, a quality control blank, an internal standard, and a matrix blank were injected to minimize spectra drift, assess LC-MS performance, and monitor overtime. All extracted tissues underwent LC-MS, whereas pooled samples were analyzed via liquid chromatography-tandem mass spectrometry (LC-MS/MS) at a constant energy ramp of 30-50V for secondary ionization to derive metabolite identifications.

Statistical and Metabolomic Profiling

All LC-MS data – mass-to-charge ratios (m/z), relative metabolite abundance, and retention time – were processed using MSConvert and Progenesis QI (Table S8). Using previously established pipelines for analysis[22, 33, 67], data underwent interquartile range normalization, log transformation, and autoscaling in MetaboAnalyst (version 6.0)[68]. Analyses performed in MetaboAnalyst to visualize metabolomic differences between injured and uninjured male and female mice across tissue types included principal component analysis (PCA), and partial least squares-discriminant analysis (PLS-DA). To distinguish populations of differentially regulated metabolite features across experimental groups, fold change, volcano plot analysis, and PLS-DA VIP Score analyses were performed. Heatmap analysis was conducted to pinpoint

clusters of metabolite features that are co-regulated and differentially regulated across experimental groups.

Populations of metabolite features distinguished by these tests were then subjected to pathway enrichment analyses using MetaboAnalyst's Functional Analysis feature where the *mummichog* algorithm is used to project metabolite features onto pathways to derive biological relevance. To do this, Kyoto Encyclopedia of Genes and Genomes (KEGG) *Mus muscis* pathway library was used as the primary reference library to reference metabolites and metabolic pathways (positive mode, mass tolerance = 5 parts per million, version 1). Significance for statistical and pathway analyses was determined using a false discovery rate (FDR)-corrected significance level of $p < 0.05$.

Metabolite Identification

Pooled samples were subjected to LC-MS/MS where ions are fragmented. This acquired fragmentation pattern can then be matched against theoretical fragmentation patterns to identify metabolites. All fragmentation data were imported, peak picked, and aligned using Progenesis QI (Nonlinear Dynamics, Newcastle UK, version 3.0). Here, Progenesis QI efficiently identifies metabolites using a computational framework that compares fragmentation patterns across various databases. For the present study, databases searched included the Human Metabolome Database (HMDB), METLIN, and ChemSpider. Once patterns are searched across databases, metabolite identities are assigned a fragmentation and overall Progenesis score. In This score is determined based on retention time, isotope distribution, and mass error. For a metabolite identification to be deemed legitimate, fragmentation and overall Progenesis scores were required to be greater than 30 and 65 (out of 100), respectively. Once identified and filtered by score, they were matched against populations of LC-MS-based features distinguished by statistical analyses to unveil potential metabolic indicators of disease as well as sexually dimorphic identities. To minimize false identifications when comparing LC-MS and LC-MS/MS metabolite features and identifications, a tolerance level of 10 parts per million was enforced.

Matrix-Assisted Laser Desorption Ionization Imaging

Sample Preparation

Whole joints selected for MALDI-MSI (n = 1 mouse/group, n = 2 joints/mouse) were removed from -80°C and prepped according to the novel protocol developed for whole joint sectioning and imaging (Fig. 7). Firstly, whole joints were thawed over ice, and the distal end of the tibia and proximal end of the femur were trimmed. Next, whole joints were embedded in warm 5% carboxymethylcellulose sodium salt (ThermoFischer, A18105-36) and 10% gelatin (Thermo Scientific, AC611995000)[58, 69] . This medium was selected over optimal cutting temperature (OCT)—which is incompatible with mass spectrometry analysis due to the presence of polyethylene glycol, a major ion suppressor. Embedded whole joints were mounted to the chuck and sagittal 8 um sections were cryosectioned using a Tissue-Tek Accu-Edge 4689 blade in a cryostat set to -30°C (OTF5000 Cryostat, Bright Instrument Co Ltd). Specifically, the medial and lateral aspects of the joint were sectioned as these are the primary sites of degeneration for this injury model[16, 70]. Because whole joints did not undergo formalin fixation or paraffin embedding, Cryofilm 3C 16 UF (SECTION-LAB, Hiroshima, Japan) was applied and adhered to the tissue block to assist in transferring sections to indium tin oxide (ITO) slides (Delta

Technologies, CB-401N, 4-10 Ω/sq, 25 x 50 mm)[71]. Sections were adhered to ITO slides using double-stick tape and then directly stored at -80°C until matrix application.

Matrix Application

An in-house sublimation apparatus (Chemglass Life Sciences, CG-3038) was used for matrix application (Fig. S8). Application using sublimation was chosen over matrix spraying because it forms smaller, more homogenous matrix crystals and lacks liquid—reducing the risk of molecule migration and is more reproducible[72]. Moreover, solvent exposure from matrix spraying can cause microcracks in bone marrow and bone[58]. Four whole joint sections were present on each ITO slide, and slides were weighed before sublimation. 300 mg of 2,5-dihydroxybenzoic acid (DHB) (Alfa Aesar, 490-79-9) was uniformly dispersed in the base of the sublimation apparatus, ITO slides were affixed to the flat bottom condenser using conductive adhesive tape, and the condenser was filled with tap water (22°C). The two glass compartments of the sublimator were assembled using an O-ring seal and connected to a vacuum pump. Tissue sections on ITO slides were sublimated at 50°C for 3 minutes under 68 mTorr vacuum, resulting in a uniform matrix layer (0.05 mg/cm^2). Optimization of matrix deposition through sublimation was determined by adjusting temperature of the hot plate, amount of matrix, and time of sublimation. Following sublimation, matrix was recrystallized using a hydration chamber with 300 uL of 5% methanol 0.1% formic acid spotted onto Whatman paper. The chamber was heated in a 37°C oven for 1 minute, then ITO slides were sealed in the chamber and heated at 37°C for 1 minute.

MALDI Image Acquisition

A Bruker AutoFlex III MALDI Time-of-Flight (TOF) mass spectrometer (Bruker Daltonics) equipped with a MTP Slide Adapater II Imaging Plate (Bruker Daltonics) was used for image acquisition. Due to the size of the sublimator and ITO slides (25 x 50 mm), two small aluminum slide trays were milled to properly fit ITO slides into the imaging plate. Using a Smartbeam Nd:YAG laser (355 nm) and Bruker FlexImaging, images were collected in positive ionization and TOF modes in the 50-1000 m/z mass range averaging 200 laser shots per pixel with a 100-um lateral resolution (range = 90%, offset = 10%, laser power = 30%). Imaging data collected were analyzed and ion images were generated using Bruker SCiLS lab.

References

1. Brown TD, Johnston RC, Saltzman CL, Marsh JL, Buckwalter JA. Posttraumatic osteoarthritis: a first estimate of incidence, prevalence, and burden of disease. J Orthop Trauma 2006; 20: 739-744.

2. Thomas AC, Hubbard-Turner T, Wikstrom EA, Palmieri-Smith RM. Epidemiology of Posttraumatic Osteoarthritis. J Athl Train 2017; 52: 491-496.

3. Gottlob CA, Baker CL, Jr., Pellissier JM, Colvin L. Cost effectiveness of anterior cruciate ligament reconstruction in young adults. Clin Orthop Relat Res 1999: 272-282.

4. Griffin LY, Albohm MJ, Arendt EA, Bahr R, Beynnon BD, Demaio M, et al. Understanding and preventing noncontact anterior cruciate ligament injuries: a review of the Hunt Valley II meeting, January 2005. Am J Sports Med 2006; 34: 1512-1532.

5. Lohmander LS, Englund PM, Dahl LL, Roos EM. The long-term consequence of anterior cruciate ligament and meniscus injuries: osteoarthritis. Am J Sports Med 2007; 35: 1756-1769.

6. Cinque ME, Dornan GJ, Chahla J, Moatshe G, LaPrade RF. High Rates of Osteoarthritis Develop After Anterior Cruciate Ligament Surgery: An Analysis of 4108 Patients. Am J Sports Med 2018; 46: 2011-2019.
7. Giugliano DN, Solomon JL. ACL tears in female athletes. Phys Med Rehabil Clin N Am 2007; 18: 417-438, viii.
8. Bruder AM, Culvenor AG, King MG, Haberfield M, Roughead EA, Mastwyk J, et al. Let's talk about sex (and gender) after ACL injury: a systematic review and meta-analysis of self-reported activity and knee-related outcomes. Br J Sports Med 2023; 57: 602-610.
9. Ardern CL, Taylor NF, Feller JA, Webster KE. Fifty-five per cent return to competitive sport following anterior cruciate ligament reconstruction surgery: an updated systematic review and meta-analysis including aspects of physical functioning and contextual factors. Br J Sports Med 2014; 48: 1543-1552.
10. Tan SH, Lau BP, Khin LW, Lingaraj K. The Importance of Patient Sex in the Outcomes of Anterior Cruciate Ligament Reconstructions: A Systematic Review and Meta-analysis. Am J Sports Med 2016; 44: 242-254.
11. Blaker CL, Ashton DM, Doran N, Little CB, Clarke EC. Sex- and injury-based differences in knee biomechanics in mouse models of post-traumatic osteoarthritis. J Biomech 2021; 114: 110152.
12. Srikanth VK, Fryer JL, Zhai G, Winzenberg TM, Hosmer D, Jones G. A meta-analysis of sex differences prevalence, incidence and severity of osteoarthritis. Osteoarthritis Cartilage 2005; 13: 769-781.
13. Faber SC, Eckstein F, Lukasz S, Muhlbauer R, Hohe J, Englmeier KH, et al. Gender differences in knee joint cartilage thickness, volume and articular surface areas: assessment with quantitative three-dimensional MR imaging. Skeletal Radiol 2001; 30: 144-150.
14. Hitt K, Shurman JR, 2nd, Greene K, McCarthy J, Moskal J, Hoeman T, et al. Anthropometric measurements of the human knee: correlation to the sizing of current knee arthroplasty systems. J Bone Joint Surg Am 2003; 85-A Suppl 4: 115-122.
15. Christiansen BA, Guilak F, Lockwood KA, Olson SA, Pitsillides AA, Sandell LJ, et al. Non-invasive mouse models of post-traumatic osteoarthritis. Osteoarthritis Cartilage 2015; 23: 1627-1638.
16. Christiansen BA, Anderson MJ, Lee CA, Williams JC, Yik JH, Haudenschild DR. Musculoskeletal changes following non-invasive knee injury using a novel mouse model of post-traumatic osteoarthritis. Osteoarthritis Cartilage 2012; 20: 773-782.
17. Wu P, Holguin N, Silva MJ, Fu M, Liao W, Sandell LJ. Early response of mouse joint tissue to noninvasive knee injury suggests treatment targets. Arthritis Rheumatol 2014; 66: 1256-1265.
18. Anderson MJ, Diko S, Baehr LM, Baar K, Bodine SC, Christiansen BA. Contribution of mechanical unloading to trabecular bone loss following non-invasive knee injury in mice. J Orthop Res 2016; 34: 1680-1687.
19. Wallace CW, Hislop B, Hahn AK, Erdogan AE, Brahmachary PP, June RK. Correlations between metabolites in the synovial fluid and serum: A mouse injury study. J Orthop Res 2022.
20. Hislop BD, Devine C, June RK, Heveran CM. Subchondral bone structure and synovial fluid metabolism are altered in injured and contralateral limbs 7 days after non-invasive joint injury in skeletally-mature C57BL/6 mice. Osteoarthritis Cartilage 2022.

21. Mickiewicz B, Heard BJ, Chau JK, Chung M, Hart DA, Shrive NG, et al. Metabolic profiling of synovial fluid in a unilateral ovine model of anterior cruciate ligament reconstruction of the knee suggests biomarkers for early osteoarthritis. J Orthop Res 2015; 33: 71-77.
22. Welhaven HD, Welfley AH, Pershad P, Satalich J, O'Connell R, Bothner B, et al. Metabolic phenotypes reflect patient sex and injury status: A cross-sectional analysis of human synovial fluid. Osteoarthritis Cartilage 2023.
23. Hahn AK, Wallace CW, Welhaven HD, Brooks E, McAlpine M, Christiansen BA, et al. The microbiome mediates epiphyseal bone loss and metabolomic changes after acute joint trauma in mice. Osteoarthritis Cartilage 2021; 29: 882-893.
24. Seeley EH, Caprioli RM. Molecular imaging of proteins in tissues by mass spectrometry. Proc Natl Acad Sci U S A 2008; 105: 18126-18131.
25. Amstalden van Hove ER, Smith DF, Heeren RM. A concise review of mass spectrometry imaging. J Chromatogr A 2010; 1217: 3946-3954.
26. Cillero-Pastor B, Eijkel GB, Kiss A, Blanco FJ, Heeren RM. Matrix-assisted laser desorption ionization-imaging mass spectrometry: a new methodology to study human osteoarthritic cartilage. Arthritis Rheum 2013; 65: 710-720.
27. Cillero-Pastor B, Eijkel G, Kiss A, Blanco FJ, Heeren RM. Time-of-flight secondary ion mass spectrometry-based molecular distribution distinguishing healthy and osteoarthritic human cartilage. Anal Chem 2012; 84: 8909-8916.
28. Peffers MJ, Cillero-Pastor B, Eijkel GB, Clegg PD, Heeren RM. Matrix assisted laser desorption ionization mass spectrometry imaging identifies markers of ageing and osteoarthritic cartilage. Arthritis Res Ther 2014; 16: R110.
29. Cillero-Pastor B, Eijkel GB, Blanco FJ, Heeren RM. Protein classification and distribution in osteoarthritic human synovial tissue by matrix-assisted laser desorption ionization mass spectrometry imaging. Anal Bioanal Chem 2015; 407: 2213-2222.
30. Yamauchi M, Terajima M, Shiiba M. Lysine Hydroxylation and Cross-Linking of Collagen. Methods Mol Biol 2019; 1934: 309-324.
31. Pornprasertsuk S, Duarte WR, Mochida Y, Yamauchi M. Overexpression of lysyl hydroxylase-2b leads to defective collagen fibrillogenesis and matrix mineralization. J Bone Miner Res 2005; 20: 81-87.
32. Saito M, Marumo K. Collagen cross-links as a determinant of bone quality: a possible explanation for bone fragility in aging, osteoporosis, and diabetes mellitus. Osteoporos Int 2010; 21: 195-214.
33. Carlson AK, Rawle RA, Wallace CW, Brooks EG, Adams E, Greenwood MC, et al. Characterization of synovial fluid metabolomic phenotypes of cartilage morphological changes associated with osteoarthritis. Osteoarthritis Cartilage 2019; 27: 1174-1184.
34. Tootsi K, Vilba K, Martson A, Kals J, Paapstel K, Zilmer M. Metabolomic Signature of Amino Acids, Biogenic Amines and Lipids in Blood Serum of Patients with Severe Osteoarthritis. Metabolites 2020; 10.
35. Ohnishi A, Osaki T, Matahira Y, Tsuka T, Imagawa T, Okamoto Y, et al. Correlation of plasma amino acid concentrations and chondroprotective effects of glucosamine and fish collagen peptide on the development of osteoarthritis. J Vet Med Sci 2013; 75: 497-502.
36. Hu Y, Wu Q, Qiao Y, Zhang P, Dai W, Tao H, et al. Disturbances in Metabolic Pathways and the Identification of a Potential Biomarker Panel for Early Cartilage Degeneration in a Rabbit Anterior Cruciate Ligament Transection Model. Cartilage 2021; 13: 1376S-1387S.

37. Ding KH, Cain M, Davis M, Bergson C, McGee-Lawrence M, Perkins C, et al. Amino acids as signaling molecules modulating bone turnover. Bone 2018; 115: 15-24.
38. Yang G, Zhang H, Chen T, Zhu W, Ding S, Xu K, et al. Metabolic analysis of osteoarthritis subchondral bone based on UPLC/Q-TOF-MS. Anal Bioanal Chem 2016; 408: 4275-4286.
39. Igari T, Tsuchizawa M, Shimamura T. Alteration of tryptophan metabolism in the synovial fluid of patients with rheumatoid arthritis and osteoarthritis. Tohoku J Exp Med 1987; 153: 79-86.
40. Kang KY, Lee SH, Jung SM, Park SH, Jung BH, Ju JH. Downregulation of Tryptophan-related Metabolomic Profile in Rheumatoid Arthritis Synovial Fluid. J Rheumatol 2015; 42: 2003-2011.
41. Leimer EM, Tanenbaum LM, Nettles DL, Bell RD, Easley ME, Setton LA, et al. Amino Acid Profile of Synovial Fluid Following Intra-articular Ankle Fracture. Foot Ankle Int 2018; 39: 1169-1177.
42. Corciulo C, Cronstein BN. Signaling of the Purinergic System in the Joint. Front Pharmacol 2019; 10: 1591.
43. Croucher LJ, Crawford A, Hatton PV, Russell RG, Buttle DJ. Extracellular ATP and UTP stimulate cartilage proteoglycan and collagen accumulation in bovine articular chondrocyte pellet cultures. Biochim Biophys Acta 2000; 1502: 297-306.
44. Gratal P, Lamuedra A, Medina JP, Bermejo-Alvarez I, Largo R, Herrero-Beaumont G, et al. Purinergic System Signaling in Metainflammation-Associated Osteoarthritis. Front Med (Lausanne) 2020; 7: 506.
45. Pinto-Cardoso R, Pereira-Costa F, Pedro Faria J, Bandarrinha P, Bessa-Andres C, Correia-de-Sa P, et al. Adenosinergic signalling in chondrogenesis and cartilage homeostasis: Friend or foe? Biochem Pharmacol 2020; 174: 113784.
46. Akasaka H, Yoshida H, Takizawa H, Hanawa N, Tobisawa T, Tanaka M, et al. The impact of elevation of serum uric acid level on the natural history of glomerular filtration rate (GFR) and its sex difference. Nephrol Dial Transplant 2014; 29: 1932-1939.
47. Mumford SL, Dasharathy SS, Pollack AZ, Perkins NJ, Mattison DR, Cole SR, et al. Serum uric acid in relation to endogenous reproductive hormones during the menstrual cycle: findings from the BioCycle study. Hum Reprod 2013; 28: 1853-1862.
48. Steinberg GR, Macaulay SL, Febbraio MA, Kemp BE. AMP-activated protein kinase--the fat controller of the energy railroad. Can J Physiol Pharmacol 2006; 84: 655-665.
49. Wang J, Li J, Song D, Ni J, Ding M, Huang J, et al. AMPK: implications in osteoarthritis and therapeutic targets. Am J Transl Res 2020; 12: 7670-7681.
50. Yi D, Yu H, Lu K, Ruan C, Ding C, Tong L, et al. AMPK Signaling in Energy Control, Cartilage Biology, and Osteoarthritis. Front Cell Dev Biol 2021; 9: 696602.
51. Purdom T, Kravitz L, Dokladny K, Mermier C. Understanding the factors that effect maximal fat oxidation. J Int Soc Sports Nutr 2018; 15: 3.
52. Yang S, Wang J. Estrogen Activates AMP-Activated Protein Kinase in Human Endothelial Cells via ERbeta/Ca(2+)/Calmodulin-Dependent Protein Kinase Kinase beta Pathway. Cell Biochem Biophys 2015; 72: 701-707.
53. Cui N, Hu M, Khalil RA. Biochemical and Biological Attributes of Matrix Metalloproteinases. Prog Mol Biol Transl Sci 2017; 147: 1-73.
54. Visse R, Nagase H. Matrix metalloproteinases and tissue inhibitors of metalloproteinases: structure, function, and biochemistry. Circ Res 2003; 92: 827-839.

55. Verma RP, Hansch C. Matrix metalloproteinases (MMPs): chemical-biological functions and (Q)SARs. Bioorg Med Chem 2007; 15: 2223-2268.
56. Lee YJ, Lee EB, Kwon YE, Lee JJ, Cho WS, Kim HA, et al. Effect of estrogen on the expression of matrix metalloproteinase (MMP)-1, MMP-3, and MMP-13 and tissue inhibitor of metalloproternase-1 in osteoarthritis chondrocytes. Rheumatol Int 2003; 23: 282-288.
57. Carlson AK, Rawle RA, Adams E, Greenwood MC, Bothner B, June RK. Application of global metabolomic profiling of synovial fluid for osteoarthritis biomarkers. Biochem Biophys Res Commun 2018; 499: 182-188.
58. Good CJ, Neumann EK, Butrico CE, Cassat JE, Caprioli RM, Spraggins JM. High Spatial Resolution MALDI Imaging Mass Spectrometry of Fresh-Frozen Bone. Anal Chem 2022; 94: 3165-3172.
59. Eveque-Mourroux MR, Emans PJ, Boonen A, Claes BSR, Bouwman FG, Heeren RMA, et al. Heterogeneity of Lipid and Protein Cartilage Profiles Associated with Human Osteoarthritis with or without Type 2 Diabetes Mellitus. J Proteome Res 2021; 20: 2973-2982.
60. Pousinis P, Gowler PRW, Burston JJ, Ortori CA, Chapman V, Barrett DA. Lipidomic identification of plasma lipids associated with pain behaviour and pathology in a mouse model of osteoarthritis. Metabolomics 2020; 16: 32.
61. Carlson AK, Rawle RA, Wallace CW, Adams E, Greenwood MC, Bothner B, et al. Global metabolomic profiling of human synovial fluid for rheumatoid arthritis biomarkers. Clin Exp Rheumatol 2019; 37: 393-399.
62. Welhaven HD, Viles E, Starke J, Wallace C, Bothner B, June RK, et al. Metabolomic profiles of cartilage and bone reflect tissue type, radiography-confirmed osteoarthritis, and spatial location within the joint. Biochem Biophys Res Commun 2024; 703: 149683.
63. Welhaven HD, Welfley AH, Pershad P, Satalich J, O'Connell R, Bothner B, et al. Metabolic phenotypes reflect patient sex and injury status: A cross-sectional analysis of human synovial fluid. Osteoarthritis Cartilage 2024; 32: 1074-1083.
64. Welhaven HD, Welfley AH, Brahmachary P, Bergstrom AR, Houske E, Glimm M, et al. Metabolomic Profiles and Pathways in Osteoarthritic Human Cartilage: A Comparative Analysis with Healthy Cartilage. Metabolites 2024; 14.
65. Little CB, Hunter DJ. Post-traumatic osteoarthritis: from mouse models to clinical trials. Nat Rev Rheumatol 2013; 9: 485-497.
66. Seifer DR, Furman BD, Guilak F, Olson SA, Brooks SC, 3rd, Kraus VB. Novel synovial fluid recovery method allows for quantification of a marker of arthritis in mice. Osteoarthritis Cartilage 2008; 16: 1532-1538.
67. Welhaven HD, Vahidi G et al. The Cortical Bone Metabolome of C57BL/6J Mice Is Sexually Dimorphic. JBMR Plus 2022; 6.
68. Pang Z, Zhou G, Ewald J, Chang L, Hacariz O, Basu N, et al. Using MetaboAnalyst 5.0 for LC-HRMS spectra processing, multi-omics integration and covariate adjustment of global metabolomics data. Nat Protoc 2022; 17: 1735-1761.
69. Nelson KA, Daniels GJ, Fournie JW, Hemmer MJ. Optimization of whole-body zebrafish sectioning methods for mass spectrometry imaging. J Biomol Tech 2013; 24: 119-127.
70. Lockwood KA, Chu BT, Anderson MJ, Haudenschild DR, Christiansen BA. Comparison of loading rate-dependent injury modes in a murine model of post-traumatic osteoarthritis. J Orthop Res 2014; 32: 79-88.

71. Kawamoto T, Kawamoto K. Preparation of thin frozen sections from nonfixed and undecalcified hard tissues using Kawamot's film method (2012). Methods Mol Biol 2014; 1130: 149-164.
72. Shanmugaraj N, Rutten T, Svatos A, Schnurbusch T, Mock HP. Fast and Reproducible Matrix Deposition for MALDI Mass Spectrometry Imaging with Improved Glass Sublimation Setup. J Am Soc Mass Spectrom 2023; 34: 513-517.

Acknowledgments

Funding: Funding for the Montana State Mass Spectrometry Facility used in this publication was made possible in part by the MJ Murdock Charitable Trust, the National Institute of General Medical Sciences of the National Institutes of Health under Award Numbers P20GM103474 and S10OD28650, and the MSU Office of Research and Economic Development. This study was funded by the National Institutes of Health under Award Numbers R01AR073964 and R01AR081489 (RKJ) and the National Science Foundation under Award Number CMMI 1554708 (RKJ).

Author contributions: Conceptualization: HDW, RKJ**;** Methodology: HDW, AHW, PB, DS, BB, RKJ**;** Investigation: HDW, AHW, DS**;** Visualization: HDW, AHW, DS**;** Supervision: DS, BB, RKJ**;** Writing—original draft: HDW, AHW**;** Writing—review & editing: HDW, AHW, PB, DS, BB, RKJ

Competing interests: Authors have no conflicts of interest to disclose. Dr. June owns stock in Beartooth Biotech and OpenBioWorks, which were not involved in this study.

Data and materials availability: All data are available in the main text and the supplementary materials.

Figures

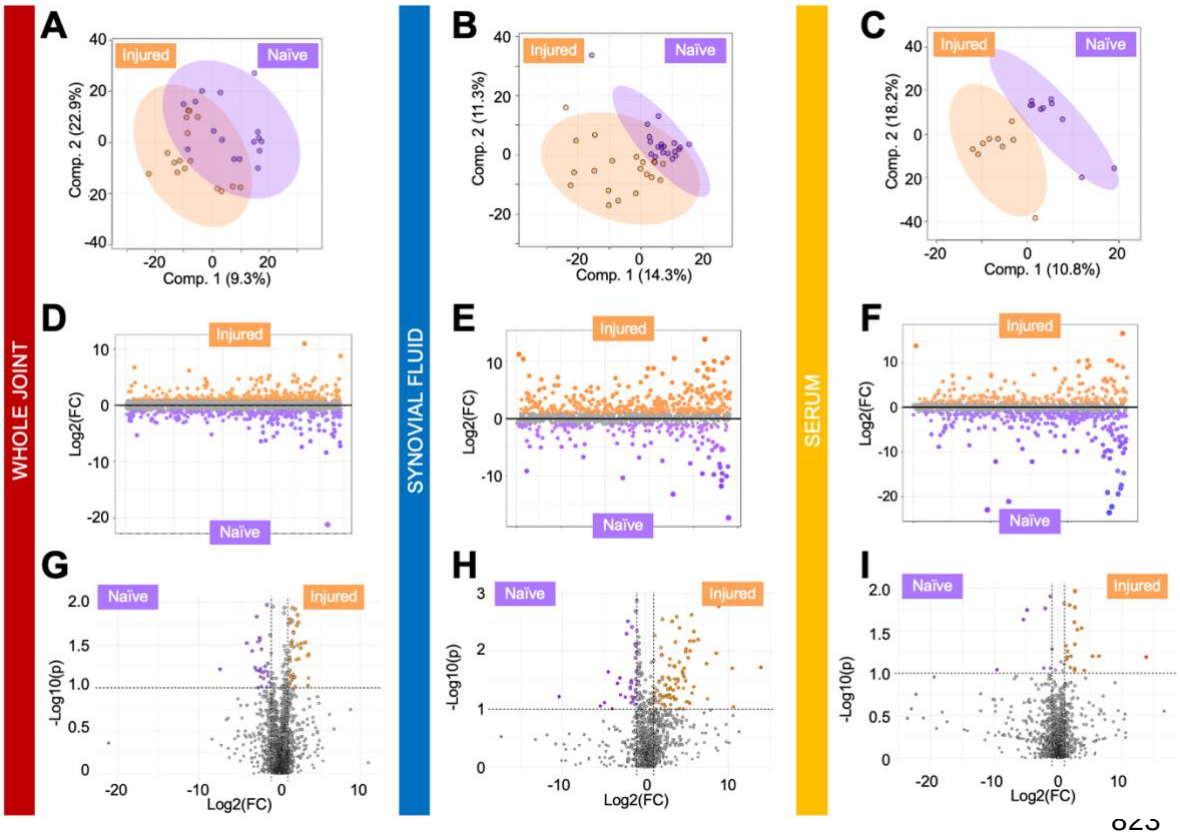

Figure 1. Global metabolomic profiles of whole joints, synovial fluid, and serum are driven by injury status. (A-C) Partial Least Squares-Discriminant Analysis (PLS-DA) finds some overlap between injured and naïve whole joint and synovial fluid and near-perfect separation of injured and naïve serum. (D-F) Fold change analysis distinguished populations of metabolite features driving separation of metabolomic profiles. (D) Specifically, 250 and 291 metabolite features were highest in injured and naïve whole joints, respectively. (E) 373 and 155 metabolite features were highest in injured and naïve synovial fluid, respectively. (F) 386 and 195 features were highest in injured and naïve serum, respectively. (G-I) To further examine metabolic differences associated with injury status across tissue types, volcano plot analysis was performed and identified numerous metabolite features that had a fold change > 2, a p-value < 0.05, and were differentially regulated between injured and naïve whole joints (G, n = 70), synovial fluid (H, n = 131), and serum (I, n = 26). The colors in A-I correspond to: purple = naïve, orange = injured, tissues - red = whole joint, blue = synovial fluid, yellow = serum.

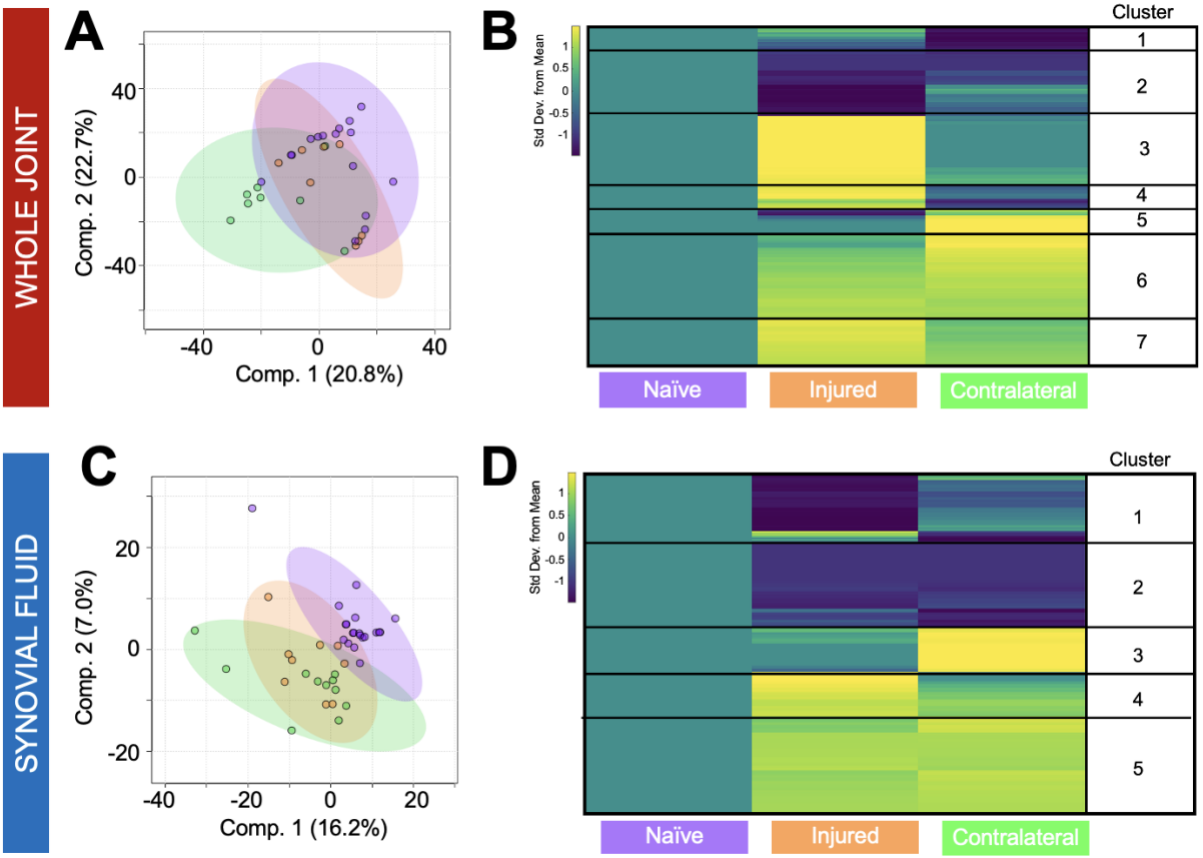

Figure 2. Distinct metabolomic profiles exist between injured, contralateral, and naïve limbs. Partial Least Squares-Discriminant Analysis (PLS-DA) reveals overlap between injured, contralateral, and naïve (A) whole joints and (C) synovial fluid with injured samples clustering together between contralateral and naïve samples. To pinpoint pathways driving metabolomic differences between limbs with different injury statuses, median intensity heatmap analyses where injured and contralateral limbs were normalized to naïve limbs were performed. Clusters of co-regulated metabolite features within (B) whole joint and (D) synovial fluid samples were subjected to pathway analyses to identify biological pathways that differ in regulation across limbs in both whole joint and synovial fluid samples. Combined, data provide strong evidence of distinct metabolomic regulation associated with injury status. Columns represent limbs (naïve, injured, contralateral) and rows represent metabolite features. Cooler and warmer colors indicate lower and higher metabolite abundance relative to the mean, respectively. Colors in A-D correspond to: naïve = purple, orange = injured, green = contralateral.

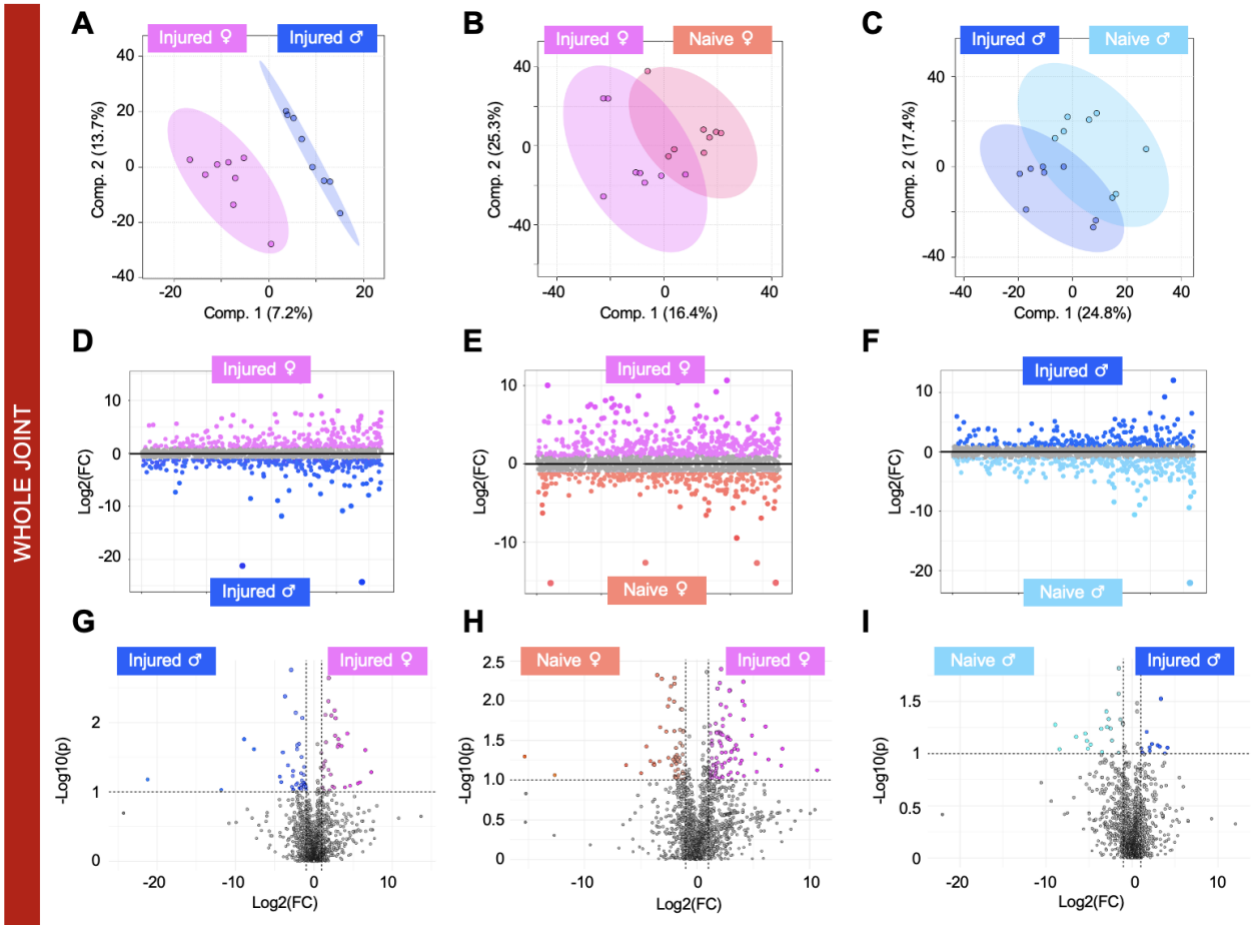

Figure 3. Whole joint metabolome differs by sex and injury. (A-C) Partial Least Squares-Discriminant Analysis (PLS-DA) finds (A) complete separation of injured whole joints from males and females and minimal overlap when comparing (B) female and (C) male injured and naïve mice. (D-F) Fold change analysis distinguished populations of metabolite features driving separation of metabolomic profiles. (D) Specifically, 315 and 314 metabolite features were highest in injured females and males, respectively. (E) 509 and 319 metabolite features were highest in injured females and naïve females, respectively. (F) 242 and 288 features were highest in injured males and naïve males, respectively. (G-I) To further examine metabolic differences associated with injury and sex, volcano plot analysis was performed and identified numerous metabolite features that had a fold change > 2, a p-value < 0.05, and were differentially regulated between injured males and females (G, n = 110), injured and naïve females (H, n = 158), and injured and naïve males (I, n = 32). The colors in A-I correspond to: pink = injured females, peach = naïve females, royal blue = injured males, light blue = naïve males.

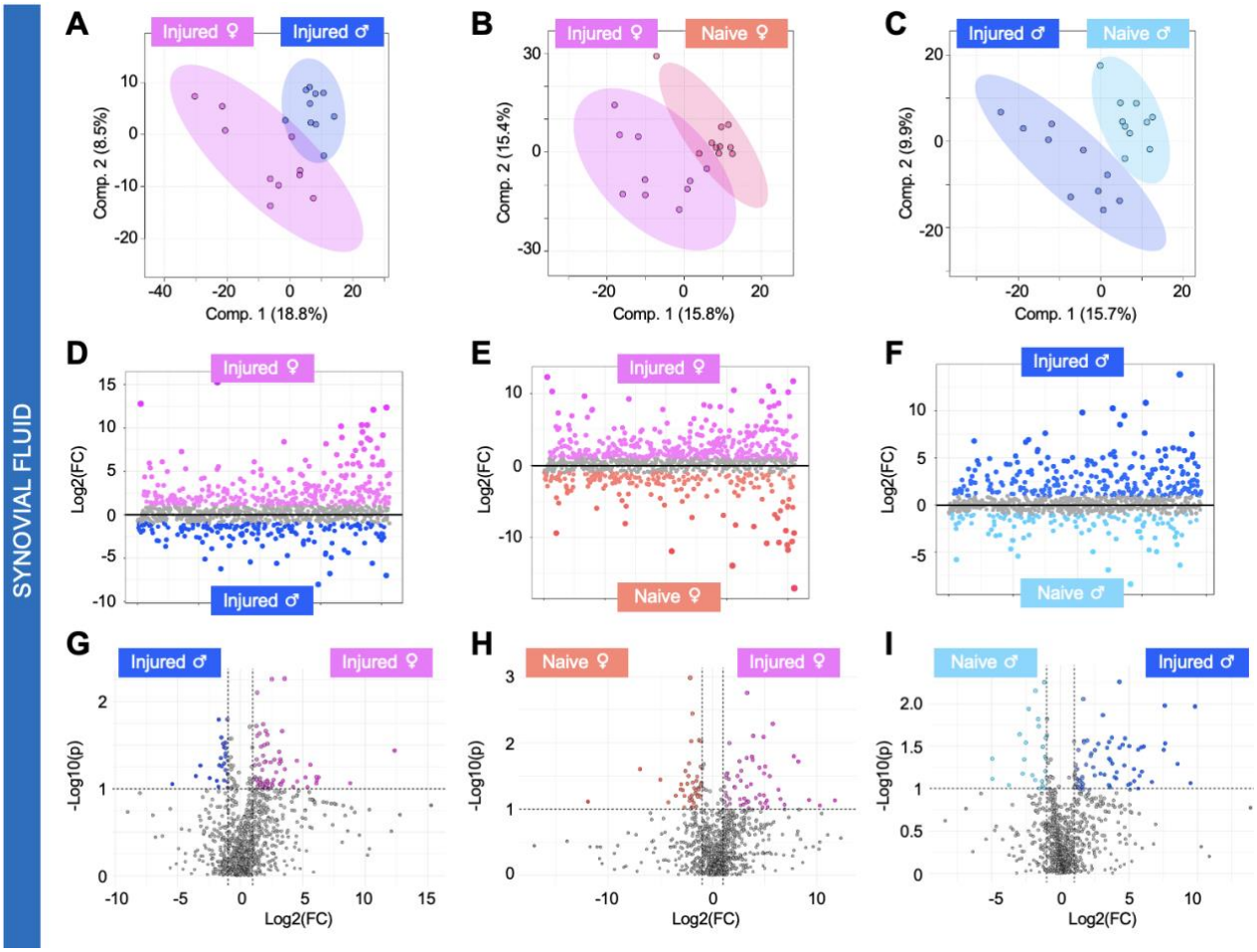

Figure 4. Metabolomic profiles of synovial fluid show sexual dimorphism across injured and uninjured mice. (A-C) Partial Least Squares-Discriminant Analysis (PLS-DA) finds minimal overlap when comparing (A) injured SF from males and females, (B) female and (C) male injured and naïve mice. (D-F) Fold change analysis identified populations of metabolite features driving separation of metabolomic profiles. (D) Specifically, 335 and 175 metabolite features were highest in injured females and males, respectively. (E) 386 and 195 metabolite features were highest in injured females and naïve females, respectively. (F) 253 and 115 features were highest in injured males and naïve males, respectively. (G-I) To further examine metabolic differences associated with injury and sex among SF samples, volcano plot analysis was performed and identified numerous metabolite features that had a fold change > 2, a p-value < 0.05, and were differentially regulated between injured males and females (G, n = 95), injured and naïve females (H, n = 101), and injured and naïve males (I, n = 99). The colors in A-I correspond to: pink = injured females, peach = naïve females, royal blue = injured males, light blue = naïve males.

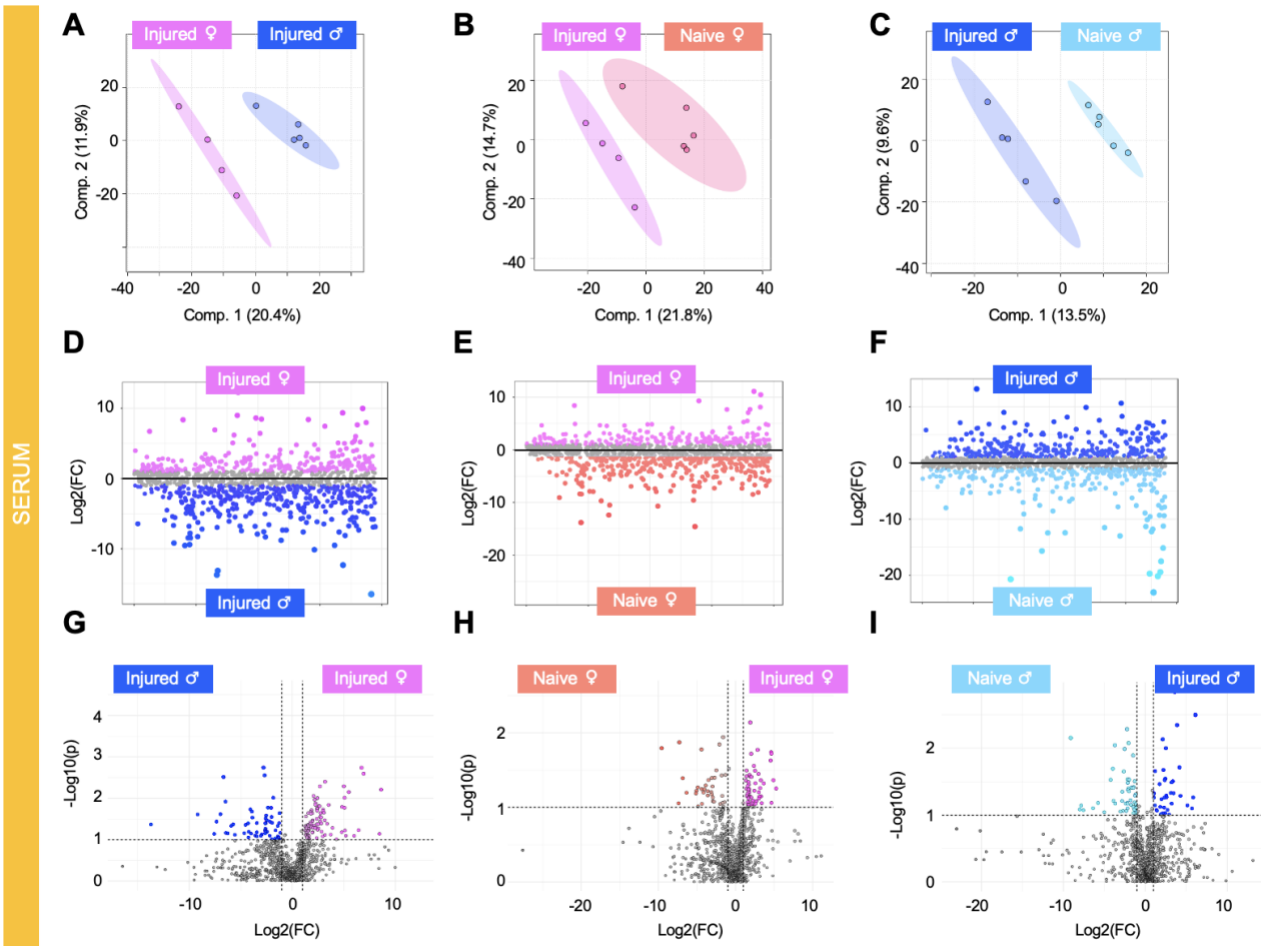

Figure 5. Serum metabolism reflects both injury status and sex. (A-C) Partial Least Squares-Discriminant Analysis (PLS-DA) finds clear separation with no overlap when comparing (A) injured SF from males and females, (B) female and (C) male injured and naïve mice. (D-F) Fold change analysis identified populations of metabolite features driving separation of serum metabolomic profiles. (D) Specifically, 267 and 407 metabolite features were highest in injured females and males, respectively. (E) 319 and 260 metabolite features were highest in injured females and naïve females, respectively. (F) 304 and 267 features were highest in injured males and naïve males, respectively. (G-I) To further examine metabolic differences associated with injury and sex across serum samples, volcano plot analysis was performed and identified numerous metabolite features that had a fold change > 2, a p-value < 0.05, and were differentially regulated between injured males and females (G, n = 82), injured and naïve females (H, n = 92), and injured and naïve males (I, n = 87). The colors in A-I correspond to: pink = injured females, peach = naïve females, royal blue = injured males, light blue = naïve males.

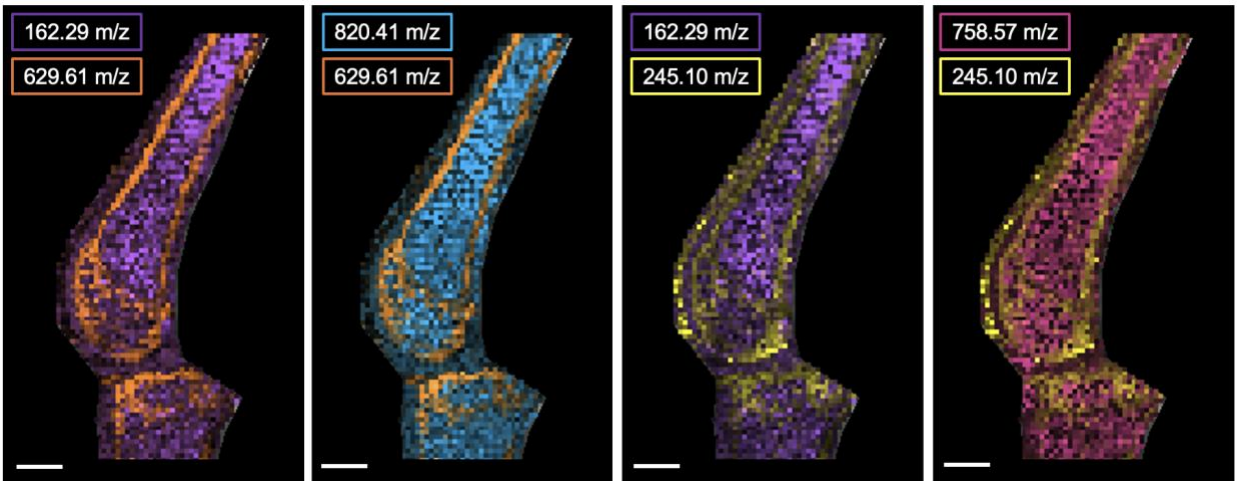

Figure 6. MALDI-MSI combined ion images from sagittal whole joint sections. Heatmap analysis of putatively identified molecular species across various tissue structures. Spatial resolution = 100 um. Scale bar = 1 mm. Interval width = 0.35 Da. Colors in panels from left to right: L-carnitine (162.29 m/z, purple), $C_{36}H_{38}O_7$ (629.61 m/z, orange), (820.41m/z, blue), hydroxyprolyl-isoleucine (245.10 m/z, yellow), and lipid species 18:2/16:0 (758.57 m/z, pink).

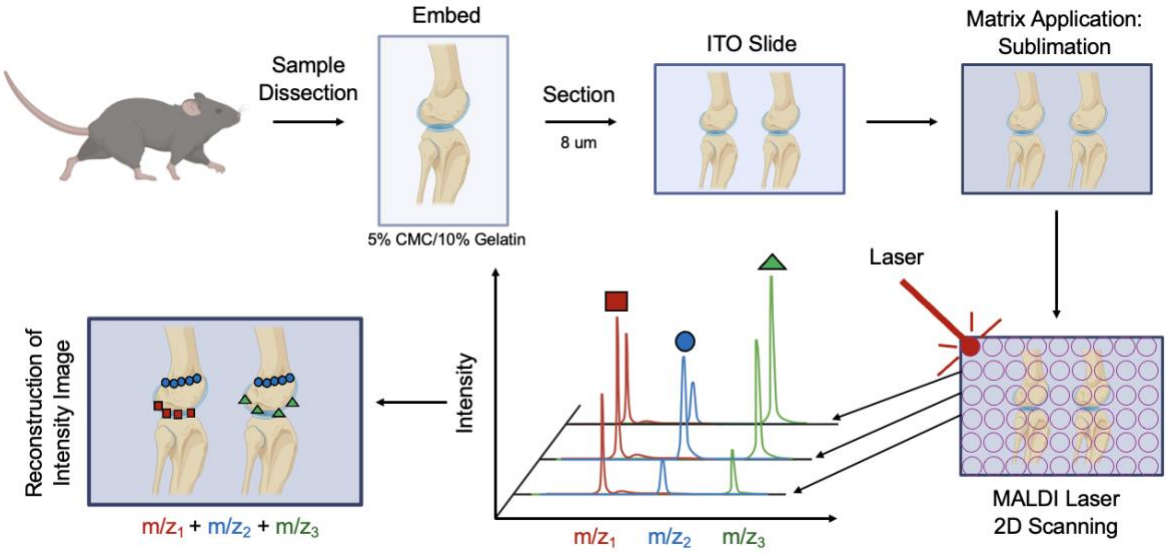

Figure 7. MALDI-MSI experimental workflow to spatially image osteochondral metabolites. Whole joints were obtained from C57Bl6/J male and female injured and naïve mice, embedded in 5% carboxylmethylcellulose (CMC)/10% gelatin, sectioned (8 um), transferred to indium tin oxide (ITO) slides, and sublimed with 2,5-dihydroxybenzoic acid matrix. Data were then acquired using 2D laser scanning followed by reconstruction of intensity images representing m/z values and intensity.

Tables

Table 1. Metabolic pathways detected in naïve and injured (A) whole joints, (B) synovial fluid, and (C) serum. All pathways listed were false discovery rate (FDR)-corrected using the Benjamini-Hochberg method.

A) Pathways detected in whole joints		
Group	Pathway	FDR p-value
Injure	Pantothenate and CoA biosynthesis	0.0241
Injure	Histidine metabolism	0.040
Naïve	Lysine degradation	0.016
Naïve	Drug metabolism - cytochrome P450	0.016
Naïve	Arginine and proline metabolism	0.018
Naïve	Terpenoid backbone biosynthesis	0.020
Naïve	Valine, leucine and isoleucine degradation	0.046
B) Pathways detected in synovial fluid		
Injured	Alanine, aspartate and glutamate metabolism	0.022
Injured	Arginine and proline metabolism	0.022
Injured	Pyrimidine metabolism	0.038
Injured	Lysine degradation	0.038
Injured	Glutathione metabolism	0.038
Injured	Arginine biosynthesis	0.044
Injured	D-Amino acid metabolism	0.044
Injured	Glycine, serine and threonine metabolism	0.046
Naïve	Biosynthesis of unsaturated fatty acids	0.018
Naïve	Purine metabolism	0.023
Naïve	Valine, leucine and isoleucine biosynthesis	0.039
Naïve	Terpenoid backbone biosynthesis	0.041
C) Pathways detected in serum		
Injured	Arginine and proline metabolism	0.034
Injured	Drug metabolism - cytochrome P450	0.032
Injured	Glutathione metabolism	0.041
Injured	Glycerophospholipid metabolism	0.029
Injured	One carbon pool by folate	0.045
Injured	Purine metabolism	0.012
Injured	Pyrimidine metabolism	0.041
Injured	Terpenoid backbone biosynthesis	0.020
Injured	Valine, leucine and isoleucine biosynthesis	0.009
Injured	Valine, leucine and isoleucine degradation	0.006
Injured	Vitamin B6 metabolism	0.020

Naïve	Arginine biosynthesis	0.019
Naïve	beta-Alanine metabolism	0.026
Naïve	D-Amino acid metabolism	0.040
Naïve	Histidine metabolism	0.014
Naïve	Nicotinate and nicotinamide metabolism	0.037

Table 2. Metabolic pathways associated with injured, contralateral, and naïve whole joints identified by median metabolite intensity heatmap analysis. Clusters defined in Figure 2B. All pathways listed were false discovery rate (FDR)-corrected using the Benjamini-Hochberg method.

Cluster	Pathway	FDR p-value
1	Nitrogen metabolism	0.039
3	Glycerophospholipid metabolism	0.027
4	Glutathione metabolism	0.038
4	Purine metabolism	0.039
5	Lysine degradation	0.030
6	Tyrosine metabolism	0.021
6	Phenylalanine, tyrosine and tryptophan biosynthesis	0.022
6	Drug metabolism - cytochrome P450	0.025
6	Ubiquinone and other terpenoid-quinone biosynthesis	0.032
7	Biosynthesis of unsaturated fatty acids	0.041
8	Glycine, serine and threonine metabolism	0.027
8	Porphyrin metabolism	0.043
8	Selenocompound metabolism	0.047
1,3	Alanine, aspartate and glutamate metabolism	0.030
1,4	Pyrimidine metabolism	0.028
1,4	Arginine biosynthesis	0.033
1,4,8	Arginine and proline metabolism	0.042
1,8	D-Amino acid metabolism	0.045
2,6	Phenylalanine metabolism	0.023
2,7,8	Valine, leucine and isoleucine biosynthesis	0.026
3,4	Histidine metabolism	0.025
7,8	Valine, leucine and isoleucine degradation	0.034

Table 3. Metabolic pathways associated with injured, contralateral, and naïve synovial fluid identified by median metabolite intensity heatmap analysis. Clusters defined in Figure 2D. All pathways listed were false discovery rate (FDR)-corrected using the Benjamini-Hochberg method.

Cluster	Pathway	FDR p-value
1	Fructose and mannose metabolism	0.046
1	Cysteine and methionine metabolism	0.046
1	Taurine and hypotaurine metabolism	0.048
1	Pyruvate metabolism	0.048
2	Tryptophan metabolism	0.016
2	Purine metabolism	0.016
2	Alanine, aspartate and glutamate metabolism	0.016
2	D-Amino acid metabolism	0.019
2	Arginine biosynthesis	0.044
3	Sphingolipid metabolism	0.020
3	Biosynthesis of unsaturated fatty acids	0.028
5	beta-Alanine metabolism	0.042
5	Glutathione metabolism	0.045
6	Pyrimidine metabolism	0.015
6	Terpenoid backbone biosynthesis	0.021
1,2	Phenylalanine metabolism	0.014
1,2	Lysine degradation	0.015
1,2	Arginine and proline metabolism	0.017
1,2	Drug metabolism - cytochrome P450	0.019
1,2	Phenylalanine, tyrosine and tryptophan biosynthesis	0.020
1,2	Tyrosine metabolism	0.038
1,4,6	Valine, leucine and isoleucine degradation	0.030
2,5	Histidine metabolism	0.040
4,5	Valine, leucine and isoleucine biosynthesis	0.049

Supplemental Results

Differences in Metabolomic Profiles Correspond to Injury Status of Joints: Pairwise Comparisons

To elucidate the systemic response following joints injury across injured, contralateral, and naïve whole joint and synovial fluid samples, PLS-DA, fold change, and volcano plot analyses were performed. Within whole joints, when comparing injured and naïve joints (Supplemental Fig. 2A), naïve and contralateral joints (Supplemental Fig. 2B), and injured and contralateral joints (Supplemental Fig. 2C) using PLS-DA some overlap is observed. However, overlap may be present due to each mouse in the study contributing both joints. Collectively, it is evident that the whole joint metabolome is influenced by injury suggesting a systemic response is produced in both injured and contralateral joints.

Further examination of these metabolic differences between joints, fold change analysis was performed to distinguish populations of metabolite features driving these detected differences between injured and naïve joints (Supplemental Fig. 2D), naïve and contralateral joints (Supplemental Fig. 2E), and injured and contralateral joints (Supplemental Fig. 2F). Populations were subjected to pathway analyses revealing numerous differentially regulated pathways across pairwise comparisons. Sphingolipid metabolism and alanine, aspartate, and glutamate metabolism were consistently highest in injured joints. Tryptophan metabolism was consistently detected in contralateral joints, whereas various amino acid pathways (lysine, arginine, proline) were consistently detected in naïve joints. In total, 16 significant pathways were detected between injured and naïve joints, 12 between contralateral and naïve joints, and 11 between injured and contralateral joints (Supplemental Table 2). Volcano plot analyses were performed to distinguish metabolite features that had a p-value < 0.05 and a fold change < 2. These metabolite features were then matched against putative identifications made using LC-MS/MS.

In a similar way, SF from injured, contralateral, and naïve joints were analyzed to elucidate if a systemic response is seen in this tissue type. PLS-DA analysis of SF samples displays minimal overlap between naïve and injured SF (Supplemental Fig. 3A), naïve and contralateral SF (Supplemental Fig. 3B), and injured and contralateral SF (Supplemental Fig. 3C) suggesting that the SF metabolome reflects injury status and injury causes shifts in metabolism in both injured and contralateral SF. Next, fold change analyses were performed to distinguish populations of metabolite features driving these differences, then features were subjected to pathway analyses to unveil biological pathways (Supplemental Fig. 3D-F, Supplemental Table 3). Various amino acid pathways (alanine, proline, alanine, aspartate, glutamate, lysine, arginine, tyrosine, phenylalanine), glycerophospholipid metabolism, and glutathione metabolism were consistently higher in injured SF. Notably, glutathione metabolism was higher in contralateral SF compared to naive SF. Glycine, serine, and threonine metabolism as well as glyoxylate and dicarboxylate metabolism were highest in contralateral SF compared to naïve and injured SF. Biosynthesis of unsaturated fatty acids and terpenoid backbone biosynthesis were highest in naïve SF compared to injured and contralateral SF. In total, 23 significant pathways were detected between injured and naïve SF, 20 between contralateral and naïve SF, and 17 between injured and contralateral SF (Supplemental Table 3). Volcano plot analyses were performed to distinguish SF-derived metabolite features that had a p-value < 0.05 and a fold change < 2. These metabolite features were then matched against putative identifications made using LC-MS/MS (Supplemental Fig. 3G-I).

Supplemental Figures

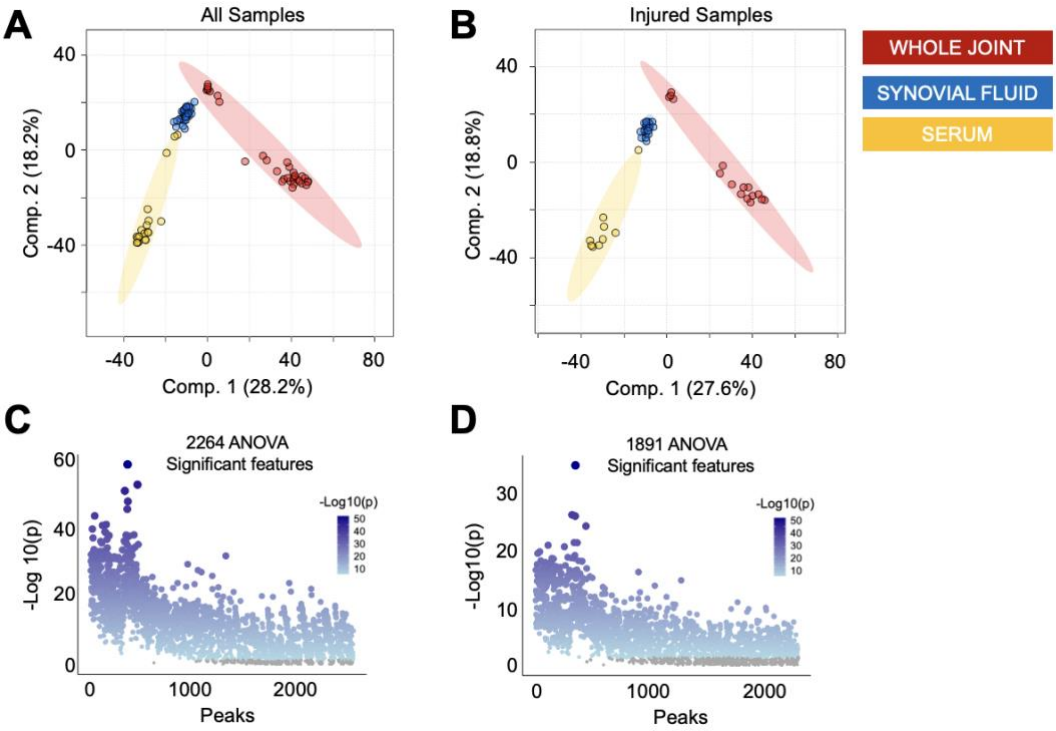

Fig. S1. The metabolome is distinct for whole joints, synovial fluid, and serum. Partial Least Squares-Discriminant Analysis (PLS-DA) of (A) all samples and (B) only samples from injured mice displays clear separation of whole joints, synovial fluid, and serum suggesting the metabolome of each tissue is substantially distinct from others. (C) ANOVA analysis identified 2,264 metabolite features that were significantly dysregulated across samples from all three tissue types. (D) When comparing samples from injured mice only, ANOVA analysis identified 1,891 significantly dysregulated features across tissue types. Colors in A-B correspond to: red = whole joint, blue = synovial fluid, yellow = serum.

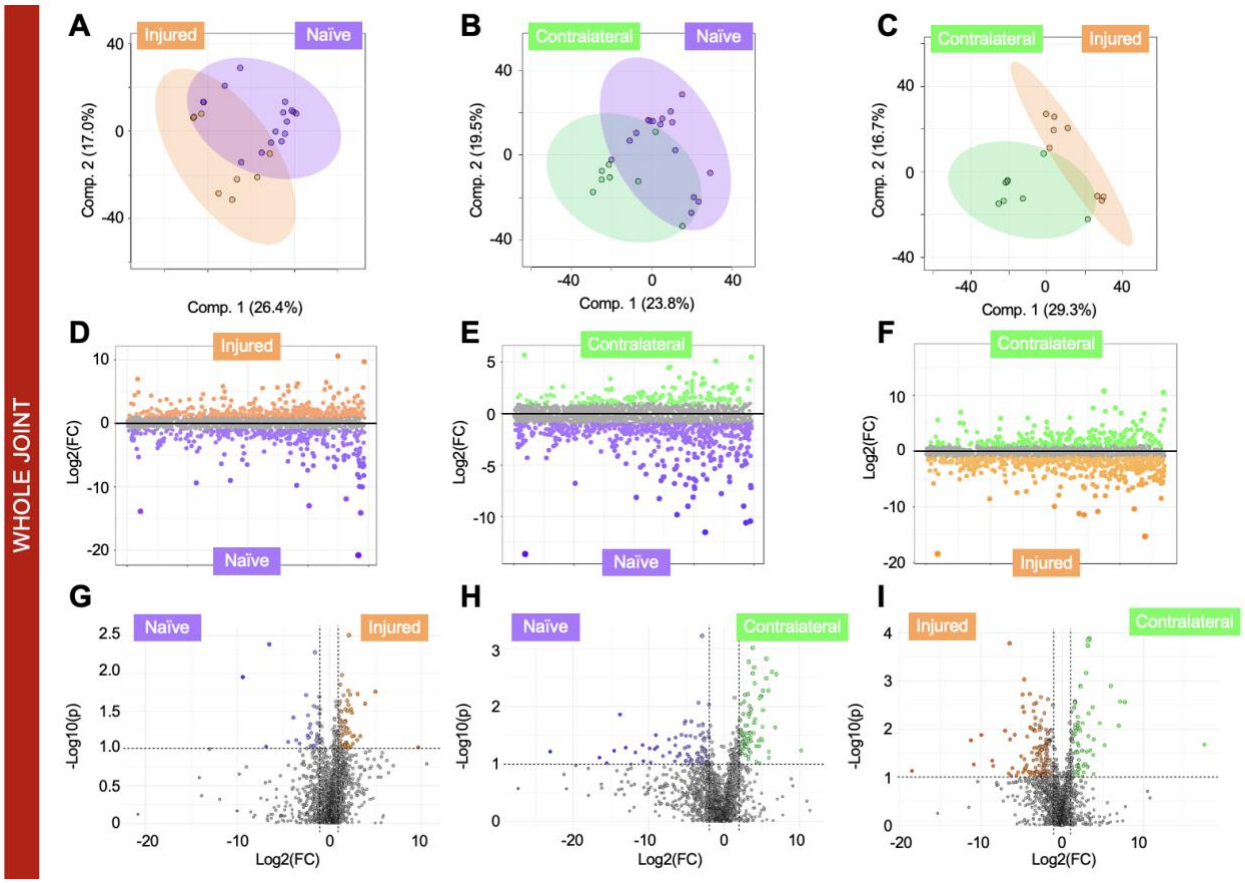

Fig. S2. Metabolomic profiles from injured, contralateral, and naïve whole joints are distinct. (A-C) Partial Least Squares-Discriminant Analysis (PLS-DA) finds some overlap between (A) injured and naïve, (B) naïve and contralateral, and (C) injured and contralateral whole joints. (D-F) Fold change analysis distinguished populations of metabolite features driving separation of metabolomic profiles. (D) Specifically, 427 and 310 metabolite features were highest in injured and naïve whole joints, respectively. (E) 182 and 496 metabolite features were highest in contralateral and naïve whole joints, respectively. (F) 236 and 571 features were highest in contralateral and injured whole joints, respectively. (G-I) To further examine metabolic differences associated with injury status across whole joints, volcano plot analysis was performed and identified numerous metabolite features that had a fold change > 2, a p-value < 0.05, and were differentially regulated between injured and naïve (G, n = 97), contralateral and naive (H, n = 179), and contralateral and injured whole joints (I, n = 268). The colors in A-I correspond to: purple = naïve whole joint, orange = injured whole joint, green = contralateral whole joint.

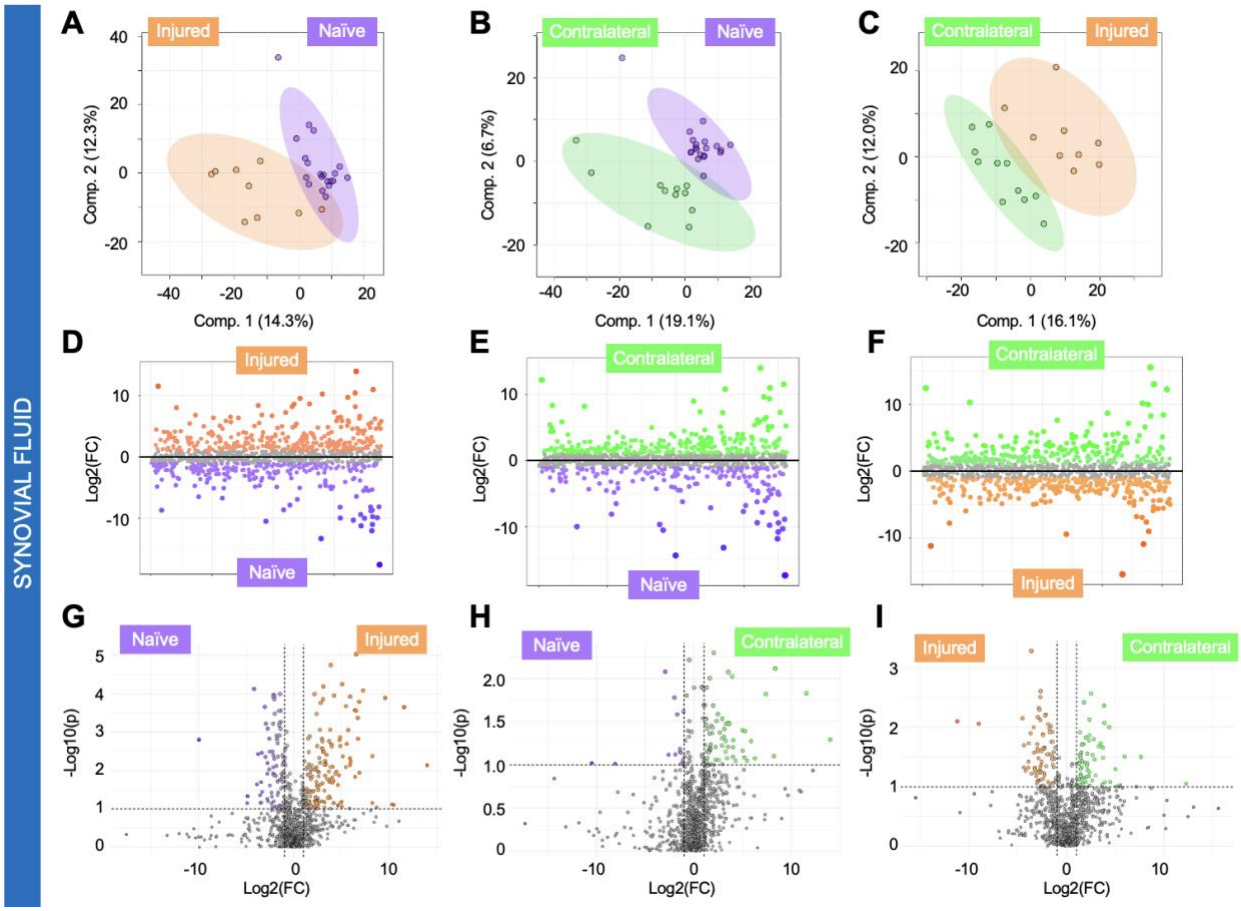

Fig. S3. Synovial fluid metabolome differs across injured, contralateral, and naïve limbs. (A-C) Partial Least Squares-Discriminant Analysis (PLS-DA) finds some overlap between (A) injured and naïve, (B) naïve and contralateral, and (C) injured and contralateral synovial fluid. (D-F) Fold change analysis distinguished populations of metabolite features driving separation of metabolomic profiles. (D) Specifically, 318 and 253 metabolite features were highest in injured and naïve synovial fluid, respectively. (E) 269 and 178 metabolite features were highest in contralateral and naïve synovial fluid, respectively. (F) 303 and 291 features were highest in contralateral and injured synovial fluid, respectively. (G-I) To further examine metabolic differences associated with injury status across whole joints, volcano plot analysis was performed and identified numerous metabolite features that had a fold change > 2, a p-value < 0.05, and were differentially regulated between injured and naïve (G, n = 59), contralateral and naive (H, n = 81), and contralateral and injured synovial fluid (I, n = 140). The colors in A-I correspond to: purple = naïve synovial fluid, orange = injured synovial fluid, green = contralateral synovial fluid.

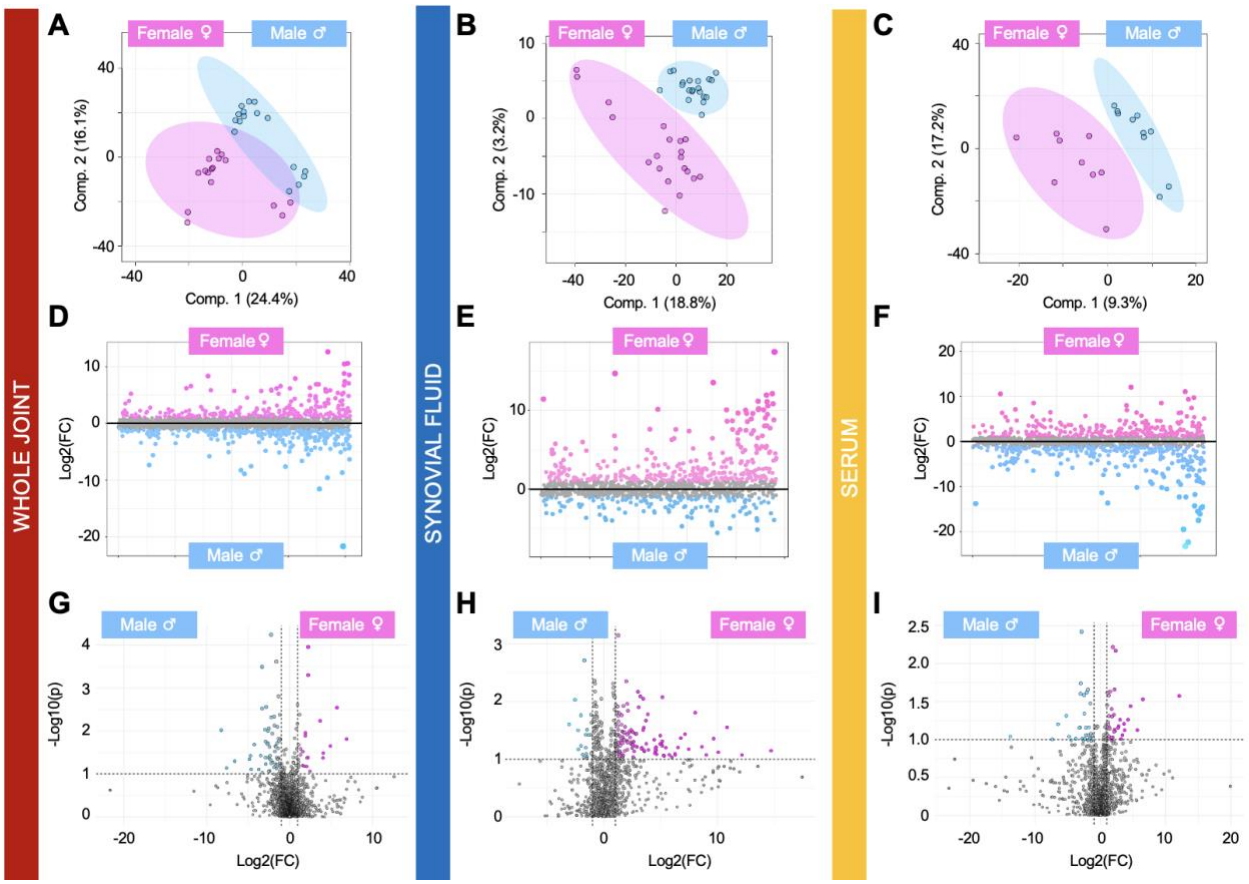

Fig. S4. Sexual dimorphic patterns are detected across whole joints, synovial fluid, and serum from injured and naïve mice. (A-C) Partial Least Squares-Discriminant Analysis (PLS-DA) finds (A) minimal overlap of male and female whole joints, while (B) synovial fluid and (C) serum from males and females perfectly clusters apart from each other. (D-F) Fold change analysis distinguished populations of metabolite features driving separation of male and female metabolomic profiles. (D) Specifically, 253 and 314 metabolite features were highest in female and male whole joints, respectively. (E) 334 and 137 metabolite features were highest in female and male synovial fluid, respectively. (F) 267 and 315 features were highest in female and male serum, respectively. (G-I) To further examine metabolic differences associated with sex across tissue types, volcano plot analysis was performed and identified numerous metabolite features that had a fold change > 2, a p-value < 0.05, and were differentially regulated between male and female whole joints (G, n = 90), synovial fluid (H, n = 159), and serum (I, n = 63). The colors in A-I correspond to: pink = females, blue = males, red = whole joint, blue = synovial fluid, yellow = serum.

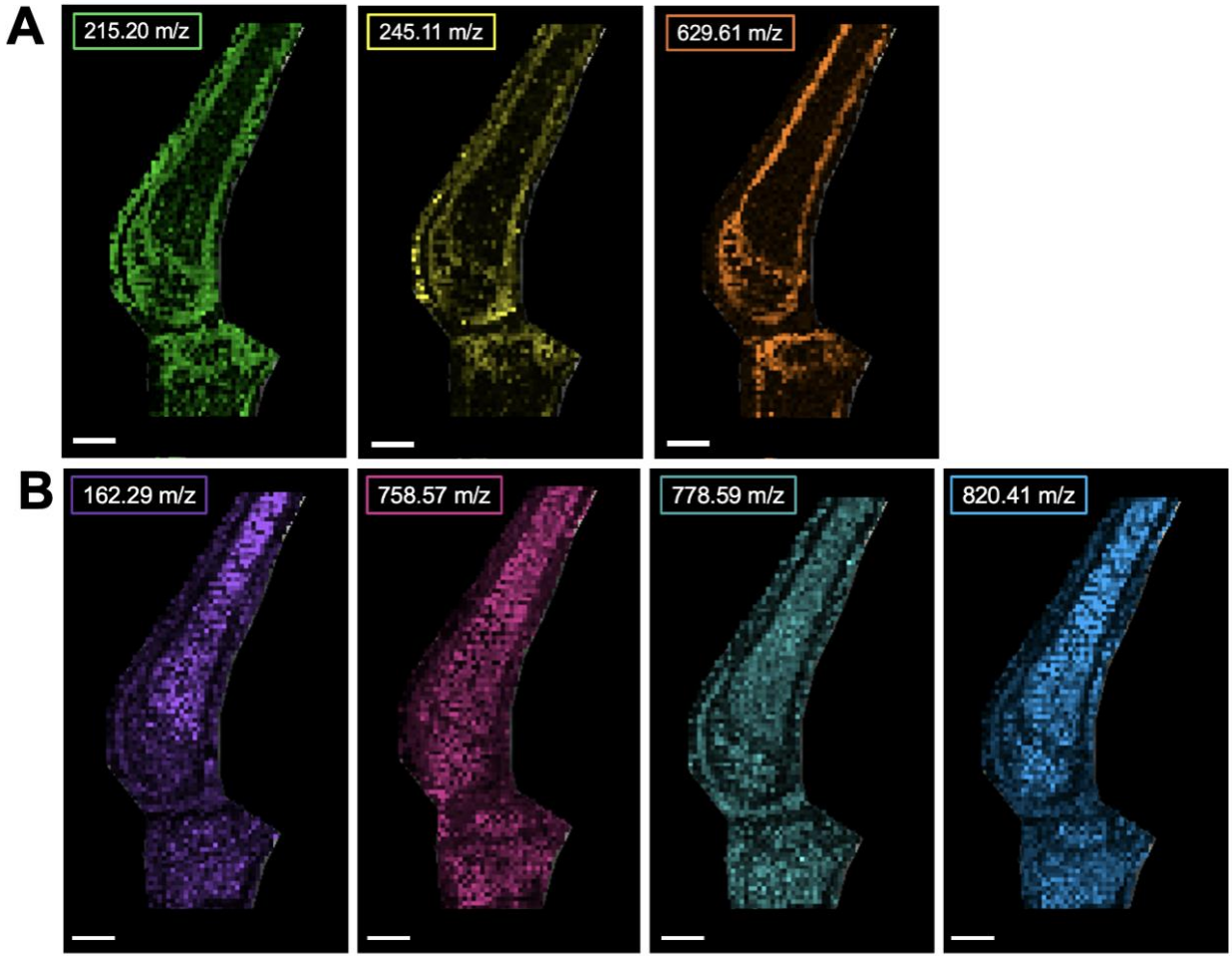

Fig. S5. MALDI-MSI analysis combined with LC-MS/MS detects and identifies differences in osteochondral metabolites. (A) Molecular species that were putatively identified with notable spatial patterns amongst bone and the growth plate include alpha-carboxy-delta-decalactone (215.20, green), hydroxyprolyl-isoleucine (245.11 m/z, yellow), and $C_{36}H_{38}O_7$ (629.61 m/z, orange). (B) conversely, molecular species that were putatively identified with notable patterns among bone marrow regions include L-carnitine (162.29 m/z, purple) and various lipid species (34 carbons, 2 double bonds – 758.57 m/z, pink; 34 double bonds, 3 double bonds – 778.59 m/z, teal; 39 carbons, 6 double bonds – 820.41 m/z, blue). Spatial resolution = 100 um. Scale bar = 1 mm. Interval width = 0.35 Da.

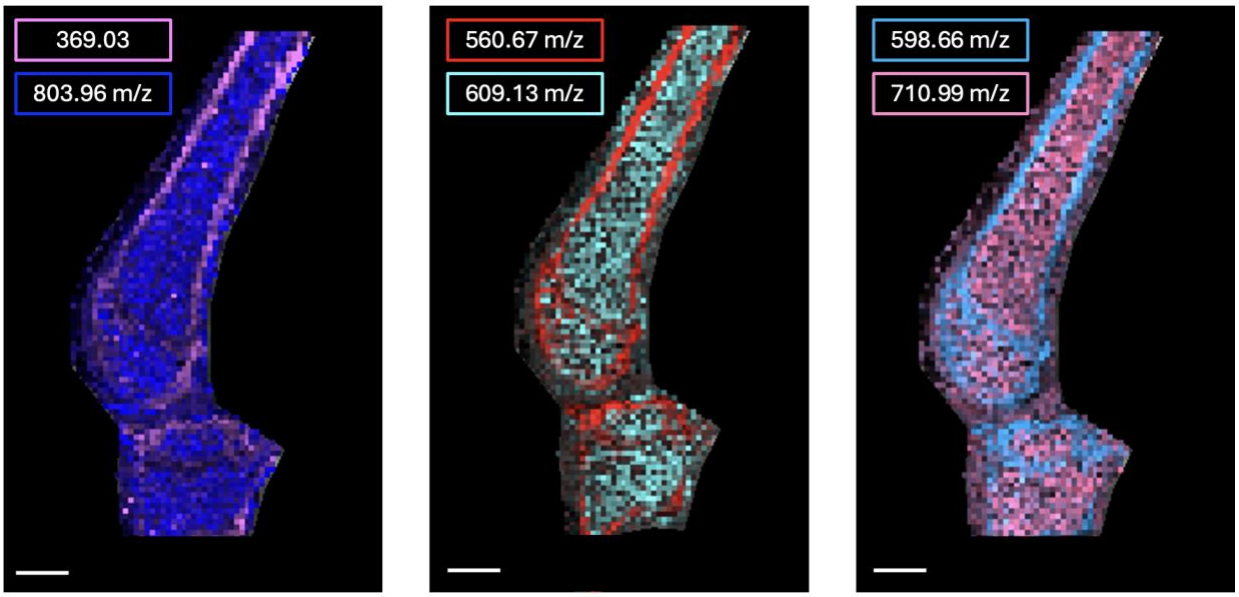

Fig. S6. Unidentified molecular species localize to different structures within the joint. Species more abundant in bone and growth plate included 369.03 m/z (pink), 560.67 m/z (red), and 598.66 m/z (light blue). Conversely, those more abundant in bone marrow included 803.96 m/z (dark blue), 609.13 m/z (cyan), and 710.99 m/z (light pink). Spatial resolution = 100 um. Scale bar = 1 mm. Interval width = 0.35 Da.

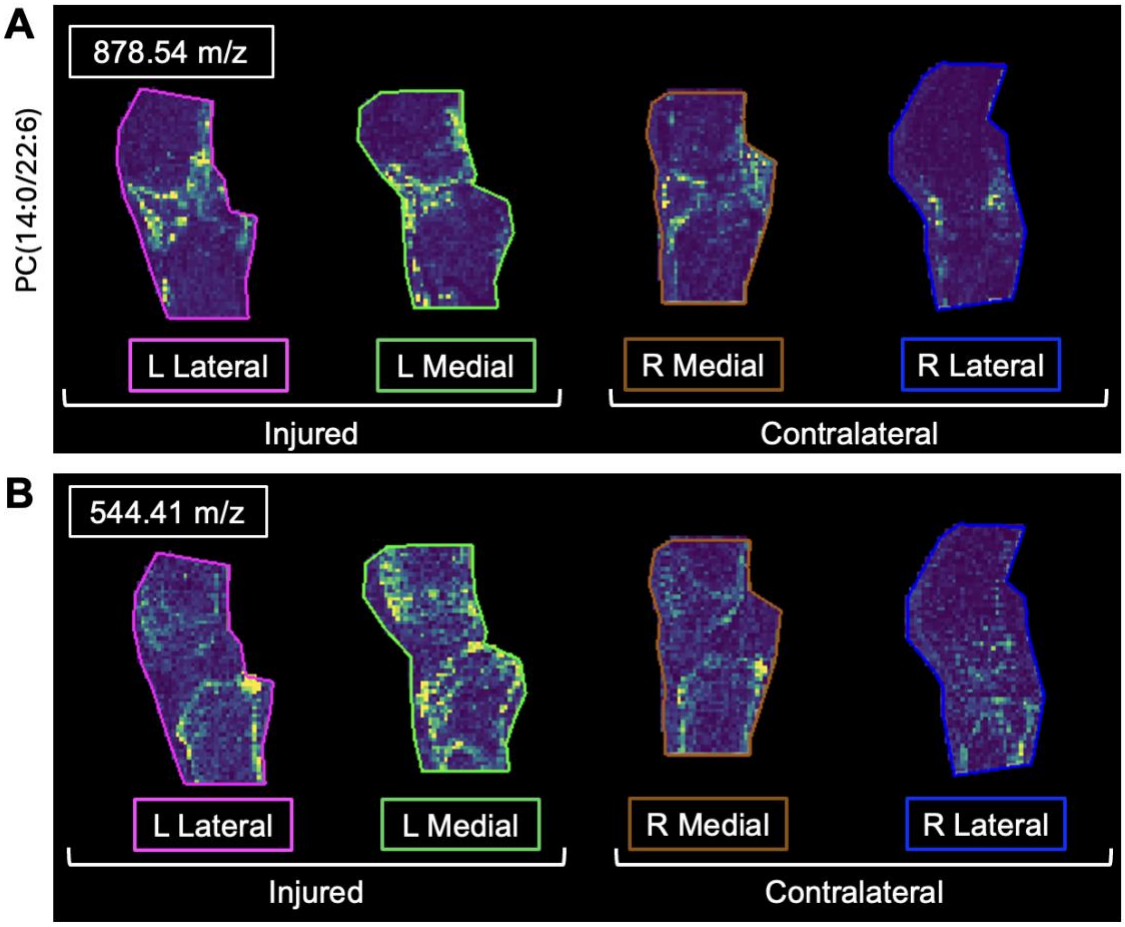

S Figure 7. Injury-associated spatial distribution patterns between injury and contralateral limbs. (A) 544.41 m/z and (B) putatively identified PC(14:0/22:6) (878.54 m/z) display notable injury associated patterns between medial and lateral sagittal sections from an injured and contralateral joint. Left to right – left lateral, left medial, right medial, right lateral. Spatial resolution = 100 um. Scale bar = 1 mm. Interval width = 0.35 Da.

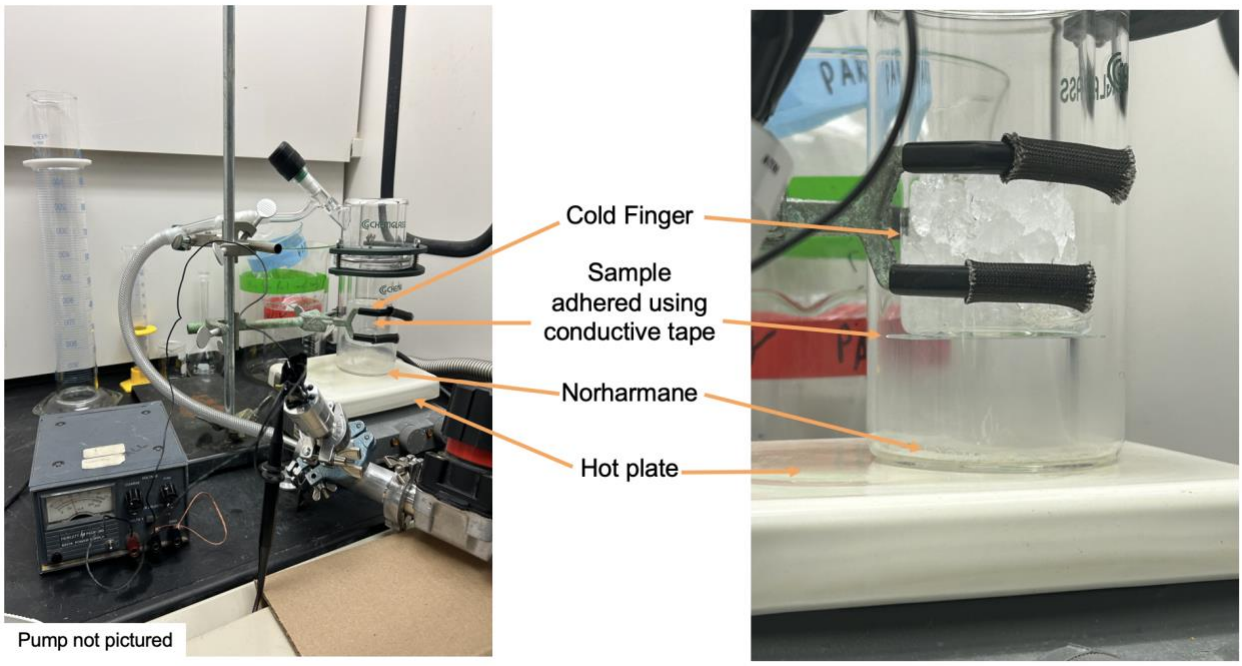

Fig. S8. Sublimation apparatus used to uniformly coat whole joints with matrix. Components of the sublimation apparatus include the cold finger, hot plate, glass condenser and sleeve, O-ring seal, and vacuum pump (not pictured).

Supplemental Tables

Table S1. Liquid chromatography tandem mass spectrometry (LC-MS/MS).derived putative metabolite identifications that differ between male and female injured mice across tissues (serum, synovial fluid, whole joints), and limbs (injured, contralateral, naïve). Provided information for putative identifications includes observed and theoretical mass-to-charge ratios (m/z), parts per million (ppm) error, compound identification, accepted description/name, adduct information, chemical formula, and scores (total, fragmentation). Identifications with an error > 10 ppm, overall score < 65, and fragmentation score < 30 were excluded.

Table S2. Differentially regulated pathways, identified by MetaboAnalyst, when comparing injured, contralateral, and naïve whole joints using fold change analysis.

Table S3. Differentially regulated pathways, identified by MetaboAnalyst, when comparing synovial fluid from injured, contralateral, and naïve limbs using fold change analysis.

Table S4. Differentially regulated pathways, identified by MetaboAnalyst, when comparing whole joints obtained from male and female injured and naïve mice using fold change analysis.

Table S5. Differentially regulated pathways, identified by MetaboAnalyst, when comparing synovial fluid from male and female injured and naïve mice using fold change analysis.

Table S6. Differentially regulated pathways, identified by MetaboAnalyst, when comparing serum from injured, contralateral, and naïve limbs using fold change analysis.

Table S7. MALDI ion data.

Table S8. Raw metabolomics output.